JFM PAPERS

Asymptotic scaling laws for periodic turbulent boundary layers and their numerical simulation up to $Re_\theta = 8300$

Andrew Wynn[1] [iD], Saeed Parvar[1], Joseph O'Connor[2] [iD], Ricardo A.S. Frantz[3] [iD] and Sylvain Laizet[1]

[1]Department of Aeronautics, Imperial College London, South Kensington Campus, London SW7 2AZ, UK

[2]EPCC, Bayes Centre, University of Edinburgh, 47 Potterrow, Edinburgh EH8 9BT, UK

[3]Arts et Métiers Institute of Technology, CNAM, DynFluid, HESAM Université, F-75013, Paris, France

Corresponding author: Andrew Wynn, a.wynn@imperial.ac.uk

We provide a rigorous analysis of the self-similar solution of the temporal turbulent boundary layer, recently proposed by Biau (2023 *Comput. Fluids* **254**, 105795), in which a body force is used to maintain a statistically steady turbulent boundary layer with periodic boundary conditions in the streamwise direction. We derive explicit expressions for the forcing amplitudes which can maintain such flows, and identify those which can hold either the displacement thickness or the momentum thickness equal to unity. This opens the door to the first main result of the paper, which is to prove upper bounds on skin friction for the temporal turbulent boundary layer. We use the Constantin–Doering–Hopf bounding method to show, rigorously, that the skin-friction coefficient for periodic turbulent boundary layer flows is bounded above by a uniform constant which decreases asymptotically with Reynolds number. This asymptotic behaviour is within a logarithmic correction of well-known empirical scaling laws for skin friction. This gives the first evidence, applicable at asymptotically high Reynolds numbers, to suggest that Biau's self-similar solution of the temporal turbulent boundary layer exhibits statistical similarities with canonical, spatially evolving, boundary layers. Furthermore, we show how the identified forcing formula implies an alternative, and simpler, numerical implementation of periodic boundary layer flows. We give a detailed numerical study of this scheme presenting direct numerical simulations up to a momentum Reynolds

number of $Re_\theta = 2000$ and implicit large-eddy simulations up to $Re_\theta = 8300$, and show that these results compare well with data from canonical spatially evolving boundary layers at equivalent Reynolds numbers.

Key words: turbulent boundary layers, Navier-Stokes equations

1. Introduction

Spatially evolving boundary layers are one of the canonical flows in fluid mechanics. Their behaviour governs the aerodynamic efficiency of aircraft, road vehicles, ships and even wind turbines via the behaviour of the atmospheric boundary layer. For this reason, there is significant interest in understanding and predicting key performance statistics, such as skin friction, of boundary layer flows. Resolved numerical simulations are a powerful tool with which to make such predictions. However, boundary layer flows of practical importance are typically at high Reynolds number, the boundary layer is itself turbulent, and the streamwise growth of its thickness necessitates a large computational domain in order to obtain converged and accurate time-averaged statistics. This places a severe restriction on the complexity of turbulent boundary layers that can be accurately simulated numerically. Indeed, Sillero, Jiménez & Moser (2013) have performed direct numerical simulations (DNS) of a turbulent boundary layer at the highest momentum Reynolds number to date, at $Re_\theta \approx 6500$, and this is at least an order of magnitude below that of the boundary layer on the fuselage of a commercial airliner flying at cruise velocity.

Owing to the computational demands of simulating spatially developing turbulent flows, there has been a growing interest in temporal-based solutions. This involves, where possible, reframing a spatially developing problem into a temporally developing one, thus enabling a homogeneous solution in the streamwise direction. This simplifies the streamwise boundary conditions, which now become periodic, and also permits a shorter domain in the streamwise direction, thus reducing the computational cost. Such an approach has been adopted for a variety of flow problems, including mixing layers (Rogers & Moser 1994) and planar jets (Reeuwijk & Holzner 2014). For the case of the spatially developing boundary layer, the temporal reformulation becomes equivalent to the Rayleigh problem, where an infinitely long plate is impulsively started at constant velocity.

Kozul, Chung & Monty (2016) were the first to provide a detailed analysis, using DNS, of the temporal turbulent boundary layer as a counterpart to the spatially developing version. Their analysis showed that the temporal approach is a good model for the spatially developing solution and is therefore a useful tool in the study of such flows. Furthermore, they argued via an analysis of similarity solutions that the two approaches should become asymptotically equivalent at high Reynolds numbers. However, one of the challenges with their approach is that the final boundary layer thickness for a given Reynolds number is not known *a priori*. Therefore, both the domain and mesh are over-sized/resolved for the majority of the simulation, thus increasing the computational cost. Another disadvantage is the limited time window where statistics can be collected for a given Reynolds number. This imposes the requirement of having to run an ensemble of simulations to obtain converged statistics, which further increases computational demand. Topalian *et al.* (2017) solved these issues by adapting the pioneering slow-growth formulation of Spalart (1986) from the original spatial-homogenisation approach to a temporal homogenisation more suited to the temporally developing turbulent boundary layer. However, the lack of a clearly defined temporal thickness growth rate introduced ambiguities with regards to extension

towards general boundary layers with a non-zero pressure gradient. More recently, Biau (2023) extended the work of Topalian *et al.* (2017) by combining the temporal slow-growth formulation with the assumption of self-similarity. In addition to this, the solution was also non-dimensionalised with respect to the momentum thickness, so that the temporal thickness growth can be calculated to ensure the momentum thickness remains equal to unity throughout the simulation. This temporal-homogenisation reformulation is especially efficient from a numerical perspective, since, in addition to permitting a shorter streamwise domain via periodicity, it is statistically stationary in time and homogeneous in the streamwise and spanwise directions. This allows efficient mesh design for the duration of the simulation *a priori*, as well as accelerated statistical convergence through temporal averaging and spatial averaging in both the streamwise and spanwise directions.

The approach taken by Biau (2023), which we study in this paper, is simple in that it only involves adding a single forcing term of the form

$$f(t)y\frac{\partial \boldsymbol{u}}{\partial y}, \tag{1.1}$$

to the governing Navier–Stokes equations, where y is the wall-normal co-ordinate, $\boldsymbol{u}$ is the fluid velocity and $f(t)$ is the amplitude of the forcing. One way to view this extra term is that it redirects streamwise momentum towards the boundary at $y = 0$, adding energy to the flow. This is necessary if one wants to use periodic boundary conditions in the streamwise direction since, for a boundary layer geometry, the assumption of periodicity causes artificial energy dissipation to the extent that the resulting flow would not be representative of any finite streamwise section of a canonical, spatially evolving, boundary layer. To achieve a non-trivial statistically stationary flow the forcing amplitude $f(t)$ must therefore be chosen carefully. In the numerical scheme proposed by Biau (2023), at each time step the forcing amplitude is defined implicitly via solution of an optimisation problem in order to control the value of an integral measure of the boundary layer thickness (either the displacement thickness, or momentum thickness) to be equal to a chosen fixed value, typically unity.

Given this method of creating 'boundary-layer-like' flows on a periodic domains, it is of interest to determine the extent to which the resulting flow resembles a finite section of a canonical, spatially evolving, boundary layer. In this paper, we make two contributions towards resolving this question, addressing both theoretical and numerical comparisons of periodic and spatially evolving boundary layer flows.

From the theoretical perspective, we derive rigorous bounds on the turbulent statistics of periodic boundary layer flows. Our main result is to show that an upper bound on the time-averaged skin-friction coefficient of the form $C_f \leqslant \upsilon(Re)$ holds, where (Re) is a Reynolds number based on the boundary layer thickness. The upper bound $\upsilon(Re)$ is shown to be monotonically decreasing in Re and converges to a constant

$$\lim_{Re\to\infty} \upsilon(Re) = \frac{1}{2\sqrt{2}}. \tag{1.2}$$

While the particular value of this constant is not important, we show that it is consistent with (i.e. higher than) the skin-friction values observed in numerical simulations. Of greater interest is that a uniform bound on skin friction is within a logarithmic correction of the well-known empirical frictions laws (Schlichting & Gersten 2017, p. 577) of the form

$$C_f \sim \frac{1}{(\log Re)^2}, \tag{1.3}$$

which are observed to hold for spatially evolving boundary layers for $Re \gg 1$. We show further that a logarithmic improvement to the uniform bound $C_f \leqslant \mathcal{O}(1)$ must hold if a weak assumption is made that the flow's turbulent kinetic energy grows logarithmically with Re. These are the first known bounds of this type proven to-date for boundary layer flows, with perhaps the most similar result in the literature being the bound on drag coefficient for a finite-length flat plate given by Kumar & Garaud (2020).

A key step towards proving the above theoretical bound is to alter Biau's numerical scheme for periodic turbulent boundary layers to remove the implicit definition of the forcing amplitude $f(t)$. We will show that an explicit formula for the forcing amplitude can be derived which enforces, asymptotically, a constant boundary layer thickness, and we show that this explicit formula agrees very accurately with the asymptotic forcing values arising from a numerical implementation of Biau's scheme. From the perspective of analysis, this gives a partial differential equation (PDE) which is amenable to applying the Constantin–Doering–Hopf upper bounding theory. However, from a numerical perspective it also opens the door to implementing an alternative numerical scheme to that presented in Biau (2023).

In the second main contribution of the paper, we show how the introduced numerical approach can be used in both DNS and implicit large-eddy simulation (ILES) to simulate turbulent boundary layers on periodic domains, at a much lower cost than spatially evolving boundary layers. We present a detailed analysis of the turbulent statistics of these flows for DNS up to $Re_\theta = 2000$ and ILES up to $Re_\theta = 8300$, first validating the new numerical scheme against the results of Biau (2023) for periodic turbulent boundary layers, and then comparing our results with the existing DNS of Schlatter & Orlu (2010) and Sillero *et al.* (2013), and with the ILES of Eitel-Amor, Orlu & Schlatter (2014), for canonical, spatially evolving, boundary layers.

1.1. *Problem set-up*

Suppose that a fluid with velocity $\boldsymbol{u} = u\boldsymbol{e}_x + v\boldsymbol{e}_y + w\boldsymbol{e}_z$ occupies a semi-infinite rectangular domain $\Omega = [0, L_x] \times [0, \infty) \times [0, L_z] \subset \mathbb{R}^3$, and is confined by an impermeable wall at $y = 0$ where no-slip boundary conditions are imposed. The flow is driven by a free-stream velocity $U_\infty \boldsymbol{e}_x$ infinitely far from the wall, and periodic boundary conditions are assumed in the streamwise $\boldsymbol{e}_x$ and spanwise $\boldsymbol{e}_z$ directions. Using U_∞ as a velocity scale and unity as a length scale, the non-dimensional Navier–Stokes equations for the flow are

$$\frac{\partial \boldsymbol{u}}{\partial t} + (\boldsymbol{u} \cdot \nabla)\boldsymbol{u} + \nabla p = \frac{1}{Re}\Delta \boldsymbol{u} + \boldsymbol{f},$$
$$\nabla \cdot \boldsymbol{u} = 0, \tag{1.4}$$

and, following Biau (2023), use the boundary conditions

$$\lim_{y \to \infty} \boldsymbol{u}(x, y, z, t) = 1 \cdot \boldsymbol{e}_x,$$
$$\boldsymbol{u}(x, 0, z, t) = \boldsymbol{0}, \tag{1.5}$$
$$\boldsymbol{u} \sim \text{periodic in the } \boldsymbol{e}_x \text{ and } \boldsymbol{e}_z \text{ directions.}$$

Here, $Re = (U_\infty/\nu)$ is the Reynolds number, $\boldsymbol{f}$ is a non-dimensional body force, and ν is the kinematic viscosity. The unusual choice of using unity as a length scale is motivated by the fact that the body force will be subsequently chosen to control the boundary layer thickness to unity, thus making this an appropriate spatial length scale for the problem.

To describe the boundary layer thickness on the periodic domain Ω, let the streamwise- and spanwise-averaged $\boldsymbol{e}_x$ velocity be given by
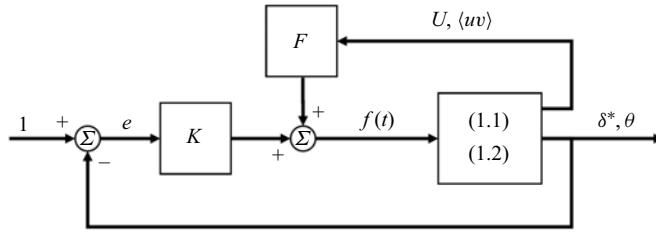
Figure 1. A schematic overview of the proposed boundary layer thickness control scheme. The idea is to force either δ^* or θ to converge to a reference value of 1, by choice of the nonlinear control laws K and F. The symbol Σ denotes the summation of two signals in the feedback loop.

$$U(y, t) := \langle u \rangle := \frac{1}{L_x L_z} \int_0^{L_x} \int_0^{L_z} u(x, y, z, t)\, \mathrm{d}x\mathrm{d}z, \qquad y, t \geqslant 0, \qquad (1.6)$$

and define the instantaneous displacement thickness, $\delta^*(t)$, and momentum thickness, $\theta(t)$, by

$$\delta^*(t) = \int_0^\infty (1 - U(y, t))\, \mathrm{d}y \quad \text{and} \quad \theta(t) := \int_0^\infty U(y, t)(1 - U(y, t))\, \mathrm{d}y. \qquad (1.7)$$

In order to control either δ^* or θ to be unity, throughout this paper we use the approach of Biau (2023) and let the body force be given by

$$\boldsymbol{f}(t) = f(t) y \frac{\partial \boldsymbol{u}}{\partial y}, \qquad (1.8)$$

where $f(t) \in \mathbb{R}$ is the forcing amplitude.

2. Boundary layer thickness control

The aim of this section is to derive explicit expressions for the forcing amplitude $f(t)$ in (1.8) under which either of the boundary layer thicknesses $\delta^*(t) \equiv 1$ or $\theta(t) \equiv 1$ can be maintained for solutions to (1.4) which satisfy the periodic boundary conditions (1.5). Figure 1 shows a schematic overview of how such a forcing $f(t)$ is defined. It consists of two components

$$f = K(e) + F(U, \langle uv \rangle), \qquad (2.1)$$

where K and F are nonlinear functionals, both of which will be defined subsequently.

The first term, K, is an error feedback controller that uses the deviation $e = e_\delta = 1 - \delta^*$ (or $e = e_\theta = 1 - \theta$) from the desired unity value of boundary layer thickness. The second term, F, which depends only on the mean streamwise velocity U and the stresses $\langle uv \rangle$, is a feed-forward control term that will be constructed from analysis of the governing equations. Importantly, this will allow us to identify an explicit formula for the forcing f once the flow is in a statistically steady state.

2.1. *Displacement thickness control*

To determine appropriate choices of the controllers K and F, first let $e_\delta(t) = 1 - \delta^*(t)$. It is shown in Appendix A that

$$\frac{\mathrm{d}e_\delta}{\mathrm{d}t} = f(t)\delta^*(t) - \frac{1}{2}C_f(t), \qquad (2.2)$$

where we define the instantaneous streamwise- and spanwise-averaged skin friction by

$$C_f(t) := \frac{2}{Re} \frac{\partial U}{\partial y}(0, t), \qquad t \geqslant 0. \tag{2.3}$$

Given (2.2), it is not difficult to see that asymptotic decay, i.e. $e_\delta(t) \to 0$, of the error can be ensured by defining the feedback and feed-forward components of the forcing amplitude $f(t)$ by

$$K(e) = -\frac{ke}{1-e} = -\frac{ke_\delta}{\delta^*}, \tag{2.4}$$

and

$$F(U) = \frac{\frac{\partial U}{\partial y}(0, t)}{Re \int_0^\infty (1 - U) \, \mathrm{d}y} = \frac{C_f}{2\delta^*}, \tag{2.5}$$

respectively, where $k > 0$ is a constant gain parameter. This observation gives the following result.

LEMMA 1. *Let $e_\delta = 1 - \delta^*$. Suppose that the forcing amplitude (1.8) is chosen such that*

$$f(t) := \frac{-ke_\delta(t) + \frac{1}{2}C_f(t)}{\delta^*(t)}, \tag{2.6}$$

for some $k > 0$. Then, for any solution to (1.4) with boundary conditions (1.5) the displacement thickness satisfies $\delta^*(t) \to 1$ as $t \to \infty$.

An important corollary of Lemma 1 is that

$$\lim_{t \to \infty} \left| f(t) - \frac{1}{2}C_f(t) \right| = 0, \tag{2.7}$$

which implies that once the flow has reached a statistically steady state it must satisfy the PDE

$$\frac{\partial \boldsymbol{u}}{\partial t} + (\boldsymbol{u} \cdot \nabla)\boldsymbol{u} + \nabla p = \frac{1}{Re} \left(\Delta \boldsymbol{u} + y \frac{\partial \boldsymbol{u}}{\partial y} \frac{\partial U}{\partial y}(0, t) \right),$$
$$\nabla \cdot \boldsymbol{u} = 0, \tag{2.8}$$

subject to the boundary conditions (1.5).

The fact that (2.8) is an explicit form of the governing equations for a periodic boundary layer flow and will be useful later in § 3.2 when discussing the dependence of the resulting flow on the forcing trajectory $f(t)$. In contrast, the numerical scheme first proposed in Biau (2023) defines the forcing $f(t)$ implicitly, via the solution to an optimisation problem, and this makes a theoretical analysis of the governing equations more challenging. Nonetheless, we will show in § 5 that a numerical implementation of (1.4) with $f(t)$ defined by either (2.6), or by using Biau's implicit method, give rise to the same flows.

2.2. *Momentum thickness control*

Momentum thickness can be controlled in an analogous manner to the displacement thickness. Letting $e_\theta(t) = 1 - \theta(t)$, it is shown in Appendix A that

$$\frac{\mathrm{d}e_\theta}{\mathrm{d}t} = f(t)\theta(t) + \frac{1}{2}C_f(t) - \frac{2}{Re}\int_0^\infty \left(\frac{\partial U}{\partial y}\right)^2 \mathrm{d}y + 2\int_0^\infty \langle uv\rangle \frac{\partial U}{\partial y}\,\mathrm{d}y. \tag{2.9}$$

In this case, the error feedback is defined by

$$K(e_\theta) = \frac{-ke_\theta}{1 - e_\theta} = \frac{-ke_\theta}{\theta}, \tag{2.10}$$

and the feed-forward term given by

$$F(U, \langle uv\rangle) = \frac{\frac{1}{Re}\frac{\partial U}{\partial y}(0) - \frac{2}{Re}\int_0^\infty \left(\frac{\partial U}{\partial y}\right)^2 \mathrm{d}y + 2\int_0^\infty \langle uv\rangle \frac{\partial U}{\partial y}\,\mathrm{d}y}{\int_0^\infty U(1 - U)\mathrm{d}y}. \tag{2.11}$$

Letting $f(t) = K(e) + F(U, \langle uv\rangle)$ and substituting into (2.9) then gives the following result.

LEMMA 2. *Let $e_\theta(t) = 1 - \theta(t)$. Suppose that the forcing amplitude (1.8) is chosen such that*

$$f(t) := \frac{-ke_\theta(t) - \frac{1}{2}C_f(t) + \frac{2}{Re}\int_0^\infty \left(\frac{\partial U}{\partial y}\right)^2 \mathrm{d}y - 2\int_0^\infty \langle uv\rangle \frac{\partial U}{\partial y}\,\mathrm{d}y}{\theta(t)}, \tag{2.12}$$

for some constant $k > 0$. Then for any solution to (1.4) satisfying the boundary conditions (1.5), the momentum thickness satisfies $\theta(t) \to 1$ as $t \to \infty$.

A consequence of Lemma 2 is that an explicit formula can be found for the asymptotic forcing

$$\lim_{t\to\infty} \left| f(t) - \left[\frac{1}{2}C_f(t) - 2\int_0^\infty \frac{1}{Re}\left(\frac{\partial U}{\partial y}\right)^2 - \frac{\partial U}{\partial y}\langle uv\rangle\,\mathrm{d}y\right]\right| = 0. \tag{2.13}$$

This result will be supported by numerical evidence presented in §5, that confirms the asymptotic limit if $f(t)$ is given either by (2.12), or computed implicitly using the method of Biau (2023).

3. Rigorous bounds on skin friction

We now address the question of whether solutions to (1.4), (1.5) on the periodic domain Ω have comparable statistical properties to those of a canonical, spatially evolving, boundary layer. In particular, our aim is to prove rigorous upper bounds on the time-averaged value of skin friction

$$C_f := \limsup_{t\to\infty} \frac{1}{T}\int_0^T C_f(t)\,\mathrm{d}t, \tag{3.1}$$

and to understand how these bounds scale with (Re). It is important to note that, even though the results of §2 ensure that the boundary layer thickness is kept constant, there is no *a priori* guarantee that the underlying fluid velocity field itself, or its statistics such as C_f, are well behaved. In other words, it is not clear that controlling a property of the flow's outer layer will necessarily give inner layer behaviour that resembles a section of a canonical, spatially evolving, boundary layer. We now investigate this question from a theoretical perspective, before presenting numerical evidence in §5.

In this section, we consider solutions to (1.4), (1.5) with the forcing $f(t)$ given by (2.6). This ensures that the displacement thickness satisfies $\delta^*(t) \to 1$ as $t \to \infty$. Consequently, the Reynolds number should be interpreted as

$$Re = Re_{\delta^*} = \frac{U_\infty \delta^*}{\nu} = \frac{U_\infty}{\nu}. \tag{3.2}$$

Throughout this section, we also only consider solutions to (1.4) that satisfy both $C_f(t) \geqslant 0$, $t \geqslant 0$, and the decay condition

$$\lim_{y \to \infty} y(e_x - u(x, y, z)) = 0, \qquad 0 \leqslant x \leqslant L_x, \ 0 \leqslant z \leqslant L_z, \tag{3.3}$$

which places only a weak constraint on the following analysis. A similar assumption was made in Kumar & Garaud (2020) when bounding the drag coefficient for flow past a finite-length flat plate.

We begin by taking the dot product of (1.4) with $u - e_x$, integrating by parts, using the boundary conditions (1.5), and the assumption (3.3) to obtain the energy equation

$$\frac{1}{2}\frac{d}{dt}\|u - e_x\|^2 + \frac{1}{Re}\|\nabla u\|^2 = \frac{1}{2}C_f(t) - \frac{1}{2}f(t)\|u - e_x\|^2, \tag{3.4}$$

a proof of which is given in Appendix A. For clarity, in the above equation, we have used the notation

$$\|u\|^2 = \int_\Omega u \cdot u \, dx. \tag{3.5}$$

Next, consider a decomposition of the velocity field

$$u(x, t) = (1 - \psi(y))e_x + v(x, t), \tag{3.6}$$

where $\psi : [0, \infty) \to \mathbb{R}$ is any function satisfying

$$\psi(0) = 1 \quad \text{and} \quad \lim_{y \to \infty} y\psi(y) = 0. \tag{3.7}$$

The perturbation $v = v_x e_x + v_y e_y + v_z e_z$ then inherits the periodic boundary conditions in the e_x, e_z directions, is incompressible, and also satisfies

$$v(x, 0, z, t) = 0 \quad \text{and} \quad \lim_{y \to \infty} yv(x, y, z, t) = 0, \tag{3.8}$$

for any fixed x, z and t.

Employing a flow decomposition of the form (3.6) is the base step of applying the 'background method' (Doering & Constantin 1992) for rigorous flow analysis. This decomposition is in terms of a 'background profile' $(1 - \psi(y))e_x$ about which perturbations v are considered. The profile ψ can be arbitrarily chosen, so long as the boundary conditions (3.7) are satisfied, and its selection is a key part of the analysis.

To explain how to select ψ in more detail, we begin with the energy equation

$$\frac{1}{2}\frac{d}{dt}\|v\|^2 = -\frac{1}{Re}\|\nabla v\|^2 + \int v_x v_y \psi' dx + \frac{1}{Re}\int \frac{\partial v_x}{\partial y}\psi' dx + f(t)\int yv \cdot \frac{\partial u}{\partial y}dx, \tag{3.9}$$

which is satisfied by the perturbations v. The meaning of each term in (3.9) can be made more transparent if it is simplified by using two identities. The first

$$\|\nabla u\|^2 = \|\nabla v\|^2 + \|\psi'\|^2 - 2\int \frac{\partial v_x}{\partial y}\psi' dx, \tag{3.10}$$

follows directly from (3.6); while the second

$$\int y\boldsymbol{v} \cdot \frac{\partial \boldsymbol{u}}{\partial y} \mathrm{d}\boldsymbol{x} = -\frac{1}{2}\|\boldsymbol{v}\|^2 - \int y v_x \psi' \mathrm{d}\boldsymbol{x}, \tag{3.11}$$

can be proven using (3.6) and the fact that $\int y\boldsymbol{v} \cdot (\partial\boldsymbol{v}/\partial y)\mathrm{d}\boldsymbol{x} = -(1/2)\|\boldsymbol{v}\|^2$ which follows from integration by parts. Upon substituting (3.10) and (3.11) into (3.9), the energy equation for the perturbations $\boldsymbol{v}$ to the background profile $(1 - \psi(y))\boldsymbol{e}_x$ is equivalent to

$$\frac{1}{2}\frac{\mathrm{d}}{\mathrm{d}t}\|\boldsymbol{v}\|^2 + \frac{1}{2Re}\big(\|\nabla\boldsymbol{v}\|^2 + \|\nabla\boldsymbol{u}\|^2\big) + \frac{1}{2}f(t)\|\boldsymbol{v}\|^2$$
$$= \frac{1}{2Re}\|\psi'\|^2 + \int v_x v_y \psi' \mathrm{d}\boldsymbol{x} - f(t)\left(\int y v_x \psi' \mathrm{d}\boldsymbol{x}\right). \tag{3.12}$$

The final two terms on the left-hand side of (3.12) are dissipative (since $f(t)$ will be chosen to be positive), while the three terms on the right-hand side provide forcing to the energy equation. The aim of the background method is to select ψ so that the forcing terms can be appropriately dominated by the dissipative terms. If this is possible then, after time averaging (3.12), one can conclude both that the perturbation energy is bounded and, furthermore, obtain quantitative bounds on the time average of the dissipative terms. Importantly, since Lemma 1 implies that $f(t) \to (1/2)C_f(t)$, this opens the door to obtaining bounds on the skin-friction coefficient of the flow.

A key challenge in applying the background method is that the magnitude of the dissipative terms in (3.12) decreases with increasing Reynolds number. Consequently, ψ must be chosen to be *Re*-dependent in such a way as to also make the forcing terms on the right-hand side of (3.12) decrease with increasing Reynolds number. The fact that the perturbations $\boldsymbol{v}$ are constructed to have homogeneous boundary conditions (3.8) is useful to achieve this. Since $\boldsymbol{v}$ is small near the boundaries, if ψ' is constructed to be non-zero only near the boundaries, then the magnitude of the final two forcing terms in (3.12) can be controlled. Ideally, one would like to pick $\psi' \equiv 0$ to eliminate all the forcing terms. However, this choice cannot be made since ψ must satisfy the boundary conditions (3.7). These state that ψ is unity at the wall and must decrease to zero far from it, which necessitates $\psi' \neq 0$. Instead, the selection of a good background profile ψ must balance the competing aims of minimising $(2Re)^{-1}\|\psi'\|^2$ (which creates energy in (3.12)), while simultaneously concentrating ψ close to the wall (which necessarily increases ψ'). Optimal choices of ψ, as will be constructed subsequently, then exhibit a natural *Re*-dependent boundary layer structure near the wall. It is important to note that the best choice of ψ for proving bounds will not necessarily correspond to any physical flow profile, such as the mean streamwise velocity.

We now proceed with the technical details for constructing a background profile ψ which achieves the aims of the previous heuristic discussion. To begin, we combine the energy equations (3.12) and (3.4) to obtain

$$\frac{\mathrm{d}}{\mathrm{d}t}\big[2\|\boldsymbol{v}\|^2 - \|\boldsymbol{u} - \boldsymbol{e}_x\|^2\big] + (C_f(t) - 2f(t))$$
$$+ 2f(t)\left(1 - \frac{1}{2}\|\boldsymbol{u} - \boldsymbol{e}_x\|^2 + \|\boldsymbol{v}\|^2 + 2\int y v_x \psi' \mathrm{d}y\right) + 2Q_\psi(\boldsymbol{v}) = \frac{2}{Re}\|\psi'\|^2, \tag{3.13}$$

where

$$Q_\psi(\boldsymbol{v}) := \frac{1}{Re}\|\nabla\boldsymbol{v}\|^2 - 2\int v_x v_y \psi' \mathrm{d}\boldsymbol{x}, \tag{3.14}$$

1020 A6-9

is a balance between dissipation and production of perturbation energy. As discussed above, the plan is to construct ψ so that the final two terms on the left-hand side of (3.13) are dissipative, i.e. such that $Q_\psi \geqslant 0$ and such that the bracketed terms multiplying the positive function f are themselves positive. After making such a choice of ψ, taking a time average of (3.13) will then facilitate a quantitative upper bound on the skin-friction coefficient since, by Lemma 1, we have $\overline{2f(t)} = C_f$. To explain precisely how time averaging the identity (3.13) leads to such an upper bound, we now discuss each of the four terms on the left-hand side of (3.13) in turn.

(i) The time average of the derivative term $(\mathrm{d}/\mathrm{d}t)[2\|\boldsymbol{v}\|^2 - \|\boldsymbol{u} - \boldsymbol{e}_x\|^2]$ is zero. This follows because it is generally true that

$$\lim_{T \to \infty} \frac{1}{T} \int_0^T \frac{\mathrm{d}g}{\mathrm{d}t} \mathrm{d}t = \lim_{T \to \infty} \frac{g(T) - g(0)}{T} = 0, \tag{3.15}$$

for any bounded function g and, using the assumption that $C_f(t) \geqslant 0$, it follows from (3.4) that both $\|\boldsymbol{u} - \boldsymbol{e}_x\|^2$ and $\|\boldsymbol{v}\|^2$ are uniformly bounded in time.

(ii) For the second term $C_f(t) - 2f(t)$, we use Lemma 1 to infer that $f(t) \to (1/2)C_f(t)$ as $t \to \infty$. Hence, taking the time average of the third term in (3.13) gives

$$\overline{C_f(t) - 2f(t)} = 0. \tag{3.16}$$

(iii) The importance of the third term

$$2f(t)\left(1 - \frac{1}{2}\|\boldsymbol{u} - \boldsymbol{e}_x\|^2 + \|\boldsymbol{v}\|^2 + 2\int y v_x \psi' \mathrm{d}y\right), \tag{3.17}$$

is that its time average will produce a term proportional to the skin-friction coefficient since, again by Lemma 1, we have $2f(t) \to C_f(t)$ as $t \to \infty$. However, a difficulty in analysing this expression is that it involves products of time-varying quantities. This difficulty can be avoided if the bracketed, flow-dependent, term multiplying $f(t)$ in (3.17) can be appropriately estimated. The aim is to show that ψ can be picked such that this term is always positive, for any velocity field $\boldsymbol{u}$ and its corresponding perturbation $\boldsymbol{v}$. Once achieved, this will imply that time averaging the term involving $f(t)$ will give a quantity proportional to the skin-friction coefficient.

To achieve this aim, first use the definition (3.6) of the perturbation $\boldsymbol{v}$ to obtain

$$\|\boldsymbol{v}\|^2 - \frac{1}{2}\|\boldsymbol{u} - \boldsymbol{e}_x\|^2 = \frac{1}{2}\|\boldsymbol{v}\|^2 + \int \psi v_x \mathrm{d}\boldsymbol{x} - \frac{1}{2}\|\psi'\|^2. \tag{3.18}$$

Hence, the bracketed term multiplying $f(t)$ in (3.17) becomes

$$1 - \frac{1}{2}\|\boldsymbol{u} - \boldsymbol{e}_x\|^2 + \|\boldsymbol{v}\|^2 + 2\int y v_x \psi' \, \mathrm{d}\boldsymbol{x}$$
$$= 1 + \frac{1}{2}\|\boldsymbol{v}\|^2 - \frac{1}{2}\|\psi\|^2 + \int v_x(\psi + 2y\psi') \, \mathrm{d}\boldsymbol{x}. \tag{3.19}$$

The final term in (3.19) can be estimated using the Cauchy–Schwarz inequality and the identity $2ab \leqslant a^2 + b^2$ by

$$\left|\int v_x(\phi + 2y\psi')\mathrm{d}\boldsymbol{x}\right| \leqslant \|v_x\|\|\psi + 2y\phi'\| \leqslant \frac{1}{2}\|v_x\|^2 + \frac{1}{2}\|\psi + 2y\psi'\|^2. \tag{3.20}$$

Using this estimate and (3.19) implies that, for any velocity field $\boldsymbol{u}$ and its corresponding perturbation $\boldsymbol{v}$,

$$1 - \frac{1}{2}\|\boldsymbol{u} - \boldsymbol{e}_x\|^2 + \|\boldsymbol{v}\|^2 + 2\int y v_x \psi' \, \mathrm{d}\boldsymbol{x}$$

$$\geqslant 1 + \frac{1}{2}\|\boldsymbol{v}\|^2 - \frac{1}{2}\|\psi\|^2 - \left|\int v_x(\phi + 2y\psi') \, \mathrm{d}\boldsymbol{x}\right|$$

$$\geqslant 1 + \frac{1}{2}\|\boldsymbol{v}\|^2 - \frac{1}{2}\|\psi\|^2 - \frac{1}{2}\|v_x\|^2 - \frac{1}{2}\|\psi + 2y\psi'\|^2$$

$$= 1 + \frac{1}{2}\left(\|v_y\|^2 + \|v_z\|^2\right) - \frac{1}{2}\left(\|\psi\|^2 + \|\psi + 2y\psi'\|^2\right)$$

$$\geqslant 1 - \frac{1}{2}\left(\|\psi\|^2 + \|\psi + 2y\psi'\|^2\right), \tag{3.21}$$

where the last inequality follows since $\|v_y\|$, $\|v_z\| \geqslant 0$. For a final simplification, expand the final term in (3.21) to obtain

$$\|\psi + 2y\psi'\|^2 = \|\psi\|^2 + 4\int y\psi\psi' \, \mathrm{d}\boldsymbol{x} + 4\|y\psi'\|^2. \tag{3.22}$$

Now, using integration by parts and the boundary conditions (3.7) on ψ

$$\int_0^\infty y\psi\psi' \, \mathrm{d}y = \left[y\psi(y)\right]_{y=0}^\infty - \|\psi\|^2 - \int_0^\infty y\psi\psi' \, \mathrm{d}y \Rightarrow \int_0^\infty y\psi\psi' \, \mathrm{d}y = -\frac{1}{2}\|\psi'\|^2. \tag{3.23}$$

Hence, using (3.21), (3.22) and (3.23) implies that the lower bound

$$\left(1 - \frac{1}{2}\|\boldsymbol{u} - \boldsymbol{e}_x\|^2 + \|\boldsymbol{v}\|^2 + 2\int y v_x \psi' \, \mathrm{d}\boldsymbol{x}\right) \geqslant 1 - 2\|y\psi'\|^2, \tag{3.24}$$

holds for any velocity field $\boldsymbol{u}$ and its corresponding perturbation $\boldsymbol{v}$.

The importance of this lower bound is that if the profile ψ is chosen such that $1 - 2\|y\psi'\|^2 > 0$, we can use the fact that $f(t) \geqslant 0$ to infer that

$$2f(t)\left(1 - \frac{1}{2}\|\boldsymbol{u} - \boldsymbol{e}_x\|^2 + \|\boldsymbol{v}\|^2 + 2\int y v_x \psi' \, \mathrm{d}\boldsymbol{x}\right) \geqslant 2f(t)(1 - 2\|y\psi'\|^2), \tag{3.25}$$

for any velocity field $\boldsymbol{u}$ and its corresponding perturbation $\boldsymbol{v}$. Time averaging the above equation, and using the fact that $|f(t) - (1/2)C_f(t)| \to 0$ from Lemma 1, then gives

$$\overline{2f(t)\left(1 - \frac{1}{2}\|\boldsymbol{u} - \boldsymbol{e}_x\|^2 + \|\boldsymbol{v}\|^2 + 2\int y v_x \psi' \, \mathrm{d}\boldsymbol{x}\right)} \geqslant C_f(1 - 2\|y\psi'\|^2), \tag{3.26}$$

where $C_f = \overline{C_f(t)}$ is the time-averaged skin-friction coefficient.

To summarise the manipulations performed so far, we have shown that time averaging (3.13) removes the first two terms on the left-hand side and, by (3.26), then gives

$$2\overline{Q_\psi(\boldsymbol{v})} + C_f(1 - 2\|y\psi'\|^2) \leqslant \frac{2}{Re}\|\psi'\|^2. \tag{3.27}$$

(iv) For the fourth term, suppose that it is possible to choose ψ such that $Q_\psi(\boldsymbol{v})$ is positive, that is,

$$Q_\psi(\boldsymbol{v}) = \frac{1}{Re}\|\nabla \boldsymbol{v}\|^2 - 2\int v_x v_y \psi' \, \mathrm{d}\boldsymbol{x} \geqslant 0, \tag{3.28}$$

holds for any vector field $\boldsymbol{v}$ satisfying the boundary conditions (3.8). Since any solution to the PDE (1.4) gives rise to such a field $\boldsymbol{v}$, it would then follow from (3.27) that

$$C_f(1 - 2\|y\psi'\|^2) \leqslant \frac{2}{Re}\|\psi'\|^2. \tag{3.29}$$

The previous four steps analysing the effect of time averaging of (3.13) imply that if ψ can be picked to satisfy the three conditions:

(C1) $Q_\psi(\boldsymbol{v}) \geqslant 0$ for any field $\boldsymbol{v}$ satisfying the boundary conditions (3.8);
(C2) $1 - 2\|y\psi'\|^2 > 0$; and
(C3) ψ satisfies the boundary conditions (3.7);

then the skin-friction coefficient must satisfy the upper bound

$$C_f \leqslant \frac{2\|\psi'\|^2}{Re(1 - 2\|y\psi'\|^2)}. \tag{3.30}$$

Given this observation, the challenge is to determine whether any profile ψ exists which satisfies the three conditions (C1)–(C3) and, if so, to find the profile which implies the tightest possible (i.e. smallest upper) bound on C_f via (3.30). Heuristically, one can observe from the definition (3.28) that if ψ' is sufficiently small then (C1) should hold. The same observation applies trivially to condition (C2) and, in addition, smaller choices of ψ' give better upper bounds via (3.30). However, as previously discussed, all of these three observations must work against the boundary conditions (C3) that ψ must satisfy.

Theorem 1, which is the main result of the paper, shows that it is possible to choose ψ to satisfy the competing constraints (C1)–(C3) and, consequently, that an upper bound on skin friction for solutions to the governing (1.4) can be proven.

THEOREM 1. *Let $Re > 1/\sqrt{2}$. For any solution of (1.4) satisfying the boundary conditions (1.5) for which $C_f(t) \geqslant 0$ and (3.3) hold, the time-averaged skin friction satisfies*

$$C_f \leqslant \frac{Re}{2(\sqrt{2}Re - 1)}. \tag{3.31}$$

Proof. Let $\psi(y)$ be defined by

$$\psi(y) = e^{-\frac{Re}{\sqrt{2}}y}, \qquad y \geqslant 0. \tag{3.32}$$

Then (C3) is satisfied since $\psi(0) = 1$ and $y\psi(y) \to 0$ as $y \to \infty$. To verify (C1), note first that for any differentiable function $f : [0, \infty) \to \mathbb{R}$ satisfying $f(0) = 0$, the Cauchy–Schwarz inequality can be used to show that

$$|f(y)| = \left|\int_0^y f'(z)\,\mathrm{d}z\right| \leqslant \sqrt{y}\left(\int_0^y |f'(y)|^2\mathrm{d}y\right)^{\frac{1}{2}}. \tag{3.33}$$

Applying this pointwise estimate to each of the velocity components v_x, v_y and using the definition of $\|\nabla\boldsymbol{v}\|^2$ then gives

$$\left|\int v_x v_y \psi'\mathrm{d}\boldsymbol{x}\right| \leqslant \frac{1}{2\sqrt{2}}\|\nabla\boldsymbol{v}\|^2\int y|\psi'(y)|\,\mathrm{d}y = \frac{1}{2Re}\|\nabla\boldsymbol{v}\|^2, \tag{3.34}$$

1020 A6-12

for any $\boldsymbol{v}$ satisfying $\boldsymbol{v}(x, 0, z) = 0$. Consequently, condition (C1) is satisfied for this choice of ψ. Finally, It then follows from (3.30) that

$$C_f \leqslant \frac{2\|\psi'\|^2}{Re(1 - 2\|y\psi'\|^2)} = \frac{Re/(2\sqrt{2})}{1 - 1/(\sqrt{2}Re)} = \frac{Re}{2(\sqrt{2}Re - 1)}. \tag{3.35}$$

$\square$

An interesting corollary of Theorem 1 can be obtained by retaining the perturbation energy term $E_{\boldsymbol{v}}(t) := (1/2)(\|v_y\|^2 + \|v_z\|^2)$ in the estimate (3.21). In Theorem 1 these terms are estimated from below by zero, but one would expect that their time average satisfies $\overline{E_{\boldsymbol{v}}} > 0$ for any turbulent solution to the governing equations. To make use of this observation, we introduce the notion of the covariance of two time series, $a(t)$ and $b(t)$, letting

$$\mathrm{cov}(a, b) := \lim_{T \to \infty} \frac{1}{T} \int_0^T (a(t) - \bar{a})(b(t) - \bar{b}) \, \mathrm{d}t. \tag{3.36}$$

It follows from this definition that the time average of the product $a(t)b(t)$ can be expressed as

$$\overline{ab} = \bar{a}\bar{b} + \mathrm{cov}(a, b). \tag{3.37}$$

Applying this formula when time averaging (3.13) then gives

$$\overline{Q_\psi(\boldsymbol{v})} + C_f\big(1 + \overline{E_{\boldsymbol{v}}} - 2\|y\psi'\|^2\big) \leqslant \frac{2\|\psi'\|^2}{Re} - \mathrm{cov}(C_f, E_{\boldsymbol{v}}). \tag{3.38}$$

We then have the following corollary, whose proof uses the same function ψ as in Theorem 1.

COROLLARY 1. *For any solution of (2.8) for which $C_f(t) \geqslant 0$ and (3.3) hold, the time-averaged skin friction satisfies*

$$C_f \leqslant \frac{1}{2\sqrt{2}(1 + \overline{E_{\boldsymbol{v}}})} - \frac{cov(C_f, E_{\boldsymbol{v}})}{1 + \overline{E_{\boldsymbol{v}}}}, \qquad Re \gg 1. \tag{3.39}$$

3.1. *Discussion of the theoretical results*

One should not expect to match the value of the constant in the analytically provable bound $C_f \leqslant (2\sqrt{2})^{-1}$ with the true value of C_f observed in numerical simulations, although numerically optimising ψ in Constantin–Doering–Hopf bounding arguments can often improve the absolute value of such constants by an order of magnitude (see, for example, studies by Plasting & Kerswell (2003) and Fantuzzi & Wynn (2016)). However, one may instead hope to capture the correct asymptotic scaling of C_f with Reynolds number. From this perspective, the result Theorem 1 is more important. That C_f is provably bounded, independent of the Reynolds number, is within a logarithmic correction of empirically observed scaling expected for spatially evolving boundary layers.

Another view is provided if we define a friction Reynolds number based on the displacement thickness by

$$Re_\tau = \frac{U_\tau \delta^*}{\nu} = Re_{\delta*}\sqrt{\frac{C_f}{2}}, \tag{3.40}$$

where $U_\tau = (\nu \overline{\partial U/\partial y(0, t)})^{1/2}$ is the friction velocity. Theorem 1 then implies that

$$Re_\tau \leqslant 2^{-\frac{5}{4}} Re_{\delta*}. \tag{3.41}$$

This is not dissimilar to the observation of Schlatter & Orlu (2010) that for canonical, spatially evolving, boundary layers

$$Re_\tau \approx cRe_{\delta*}^{0.843}, \tag{3.42}$$

where $c = 1.13(\delta^*)^{0.157}\theta^{0.843}\delta^{-1} = \mathcal{O}(1)$ is simply a constant accounting for the various possible definitions of the boundary layer thickness, and δ is the boundary layer thickness defined in terms of 99 % of the free-stream velocity.

The exponent 0.843 in this observation should be treated with caution, being based on an empirical fit to data in a small (in the context of understanding asymptotic scalings) range of Reynolds numbers. Indeed, the high Reynolds number scaling corresponding to the logarithmic friction law would be of the form

$$Re_\tau \sim \frac{Re_{\delta*}}{\log Re_{\delta*}}, \qquad Re_{\delta*} \gg 1. \tag{3.43}$$

Whether an analytical proof can bridge this 'logarithmic' gap is an important open question in theoretical fluid mechanics. It is therefore of interest that Corollary 1 provides partial evidence that the origin of such a correction can now be understood, at least for periodic boundary layers. Indeed, the improved bound

$$C_f \leqslant \frac{1}{2\sqrt{2}(1 + \overline{E_v})} - \frac{\text{cov}(C_f, E_v)}{1 + \overline{E_v}}, \tag{3.44}$$

would imply such a logarithmic correction, if it could be proven that the

$$\sup_{Re_{\delta*}>0} |\text{cov}(C_f, E_v)| < \infty \quad \text{and} \quad \lim_{Re_{\delta*}\to\infty}\left(\frac{\overline{E_v}}{\log Re_{\delta*}}\right) > 0, \tag{3.45}$$

that is, if the perturbations $\overline{E_v}$ (which, via (3.6), are defined in terms of perturbations from the constructed flow field $(1 - \psi)e_x$) themselves exhibit a logarithmic growth of energy and are only weakly correlated with the instantaneous skin friction.

3.2. *Flow dependence on the forcing amplitude $f(t)$*

Given the definitions of the forcing functions (2.6) and (2.12) for displacement and momentum control, respectively, an interesting observation is that there are many forcing amplitude trajectories $(f(t))_{t\geqslant0}$ that can achieve the desired asymptotic unity value of displacement or momentum thickness. Indeed, both (2.6) and (2.12) are parameterised by a gain $k > 0$ which gives, in each case, a whole family of forcing amplitudes which achieve asymptotic control of the boundary layer thickness. This raises the natural question of to what extent the resulting flow is dependent on the particular choice of forcing trajectory.

To begin to answer this question consider, for example, the case of displacement thickness control. It follows from (2.2) that any forcing trajectory $f(t)$ which achieves $\delta^*(t) \to 1$ must necessarily satisfy

$$\lim_{t\to\infty}\left|f(t) - \frac{1}{2}C_f(t)\right| = \lim_{t\to\infty}\left|f(t) - \frac{1}{Re}\frac{\partial U}{\partial y}(0, t)\right| = 0. \tag{3.46}$$

This implies that any forcing trajectory that achieves asymptotic convergence of the displacement thickness must converge asymptotically to the same functional form (and the formula (2.6) merely gives concrete examples of some trajectories achieving this). A more subtle question to ask, therefore, is to what extent the resulting flow is dependent on the different possible transient trajectories of $f(t)$. In other words, asking whether the nature of the journey can affect the final destination.

This is a challenging question, but we already have some evidence that supports the assertion that the eventual flow is not strongly dependent upon the transient forcing trajectory. First, the theoretical scaling law for C_f proven in Theorem 1 applies equivalently to *any* forcing trajectory that achieves $\delta^*(t) \to 1$. More generally, suppose that the forcing transient has converged in the sense that both $|f(t) - (1/2)C_f(t)|$ and $|\delta^*(t) - 1|$ are negligible. It then follows from the discussion following Lemma 1 that the flow field must satisfy the PDE (2.8). Importantly, the form of this PDE is independent of the choice of forcing trajectory, since it depends only on the asymptotic functional form $(Re)^{-1}U_y(0, t)$. Consequently, the dependence of the solution of (1.4) upon the transient forcing trajectory $f(t)$ is equivalent to considering solutions to forcing-independent PDE (2.8) initialised from different initial conditions satisfying $\delta^*(0) = 1$.

It is in this subtle sense that solutions to the periodic boundary layer equations (1.4) are independent of the forcing function $f(t)$. Of course, one would hope that (2.8) is ergodic in the sense that solutions initialised from an appropriate subset of initial conditions all have the same time-averaged statistics. However, this is a deep question in pure mathematics, which still remains open for the three-dimensional Navier–Stokes equations, and will require significant future work to resolve.

4. Numerical implementation

To perform DNS and ILES of the periodic boundary layer equations (1.4) we use the `Xcompact3d` framework, a suite of fluid flow solvers dedicated to the study of turbulent flows on supercomputers (Bartholomew *et al.* 2020), which has been extensively validated for wall-bounded turbulent flows (Diaz-Daniel, Laizet & Vassilicos 2017; Mahfoze & Laizet 2021; O'Connor *et al.* 2023). The ILES are based on a strategy that introduces targeted numerical dissipation at the small scales through the discretisation of the second derivatives of the viscous terms (Lamballais, Fortuné & Laizet 2011; Dairay *et al.* 2017). It was shown in these studies that it is possible to design a high-order finite-difference scheme in order to mimic a subgrid-scale model for ILES based on the concept of spectral vanishing viscosity, at no extra computational cost and with excellent performance for wall-bounded turbulent flows (Mahfoze & Laizet 2021).

The incompressible flow solver within `Xcompact3d` is based on sixth-order compact finite-difference schemes (Laizet & Lamballais 2009) for the spatial discretisation and a fractional-step method using a semi-implicit approach that combines the Crank–Nicholson and third-order Adams–Bashforth methods. Within the fractional-step method, the incompressibility condition is dealt with by directly solving a Poisson equation in spectral space using three-dimensional (3-D) fast Fourier transforms (FFTs) and the concept of the modified wavenumber (Lele 1992). The velocity-pressure mesh arrangement is half-staggered to avoid spurious pressure oscillations (Laizet & Lamballais 2009).

The simplicity of the mesh allows an easy implementation of a 2-D domain decomposition based on pencils (Laizet & Ning 2011). The computational domain is split into a number of sub-domains (pencils) which are each assigned to an MPI-process. The derivatives and interpolations in the x-direction (y-direction, z-direction) are performed in X-pencils (Y-pencils, Z-pencils), respectively. The 3-D FFTs required by the Poisson solver are also broken down as a series of 1-D FFTs computed in one direction at a time. Global transpositions to switch from one pencil to another are performed with the MPI command `MPI_ALLTOALL(V)`. The flow solvers within `Xcompact3d` can scale well with up to hundreds of thousands of MPI-processes for simulations with several billion mesh nodes (Laizet & Ning 2011; Bartholomew *et al.* 2020). All the simulations in this study were carried out on ARCHER2, the UK supercomputing facility. It is equipped with nodes

based on dual AMD EPYC^{TM} 7742 processors running at 2.25 GHz, totalling 128 cores per node.

In this numerical study, the following incompressible Navier–Stokes equations are solved

$$\frac{\partial \boldsymbol{u}}{\partial t} + \frac{1}{2}[\boldsymbol{\nabla} \cdot (\boldsymbol{u} \otimes \boldsymbol{u}) + (\boldsymbol{u} \cdot \boldsymbol{\nabla})\boldsymbol{u}] = -\boldsymbol{\nabla} p + (I - \boldsymbol{\Gamma})\mathcal{D}_1 + \boldsymbol{\Gamma}\mathcal{D}_2 + \boldsymbol{f}(t),$$

$$\boldsymbol{\nabla} \cdot \boldsymbol{u} = 0.$$

(4.1)

With a slight abuse of notation, $\mathcal{D}_1$ indicates that the diffusion term $\nu\Delta\boldsymbol{u}$ is directly implemented using a conventional sixth-order finite-difference scheme for its second-order spatial derivatives; while $\mathcal{D}_2$ refers to a numerical implementation of $\nu\Delta\boldsymbol{u}$ which adds targeted numerical dissipation at small scales via a customised sixth-order finite-difference scheme. Full details can be found in Lamballais *et al.* (2011), Dairay *et al.* (2017) and Mahfoze & Laizet (2021). The operator $\boldsymbol{\Gamma}$ is used to balance the weight of the two diffusive terms and can depend on the both local geometry and flow velocities via $(\boldsymbol{\Gamma}\boldsymbol{u})(x) = \Gamma(x, \boldsymbol{u})\boldsymbol{u}(x)$, where $\Gamma(x, \boldsymbol{u}) \in \mathbb{R}^{3\times 3}$. The choice $\Gamma = 0$ corresponds to a DNS implementation, in which (4.1) is mathematically equivalent to (1.4). The case $\Gamma = I$ corresponds to ILES, for which, the unknowns $\mathbf{u}(x, t)$ and $p(x, t)$ should be interpreted as the large-scale component of velocity and pressure. Note finally that the advection terms in (4.1) are written in skew-symmetric form in order to reduce aliasing errors (Kravchenko & Moin 1997).

4.1. *Numerical implementation of the forcing term*

To allow for a validation with the numerical study of Biau (2023), we will perform simulations in the case of momentum thickness control (see § 2.2) where the forcing amplitude $f(t)$ is given by (2.12). The distinction between the two considered numerical methods (i.e. DNS and ILES) introduces an extra subtlety in terms of how $f(t)$ must be chosen to achieve a desired unity value of the momentum thickness. For DNS, we use the explicit formula (2.12), letting

$$f(t) = f_{DNS}(t) := \frac{-ke_\theta(t) - \frac{1}{2}C_f(t) + \frac{2}{Re}\int_0^\infty \left(\frac{\partial U}{\partial y}\right)^2 \mathrm{d}y - 2\int_0^\infty \langle uv\rangle \frac{\partial U}{\partial y}\,\mathrm{d}y}{\theta(t)}.$$

(4.2)

Lemma 2 then guarantees that $\lim_{t\to\infty}\theta(t) = 1$ for any solution to PDE (1.4), meaning that one would expect a DNS of (4.1) to have the same behaviour. We show in § 5 that this is indeed the case.

In the case of ILES it is not appropriate to define the forcing amplitude by (2.12) since this expression is only accurate for solutions of the Navier–Stokes equations (1.4), while ILES only gives an approximate solution via (4.1). This subtlety can be avoided by adding an 'integral control' term to the forcing and using

$$f_{ILES}(t) := f_{DNS}(t) - k^2 \frac{z(t)}{\theta(t)},$$

(4.3)

where $z(t) \in \mathbb{R}$ is defined as the integral of the momentum thickness via

$$\frac{\mathrm{d}z}{\mathrm{d}t} = e_\theta(t) = 1 - \theta(t).$$

(4.4)

This accounts, with the addition of only one extra scalar-valued variable, for the small difference between the theoretical value (2.12) and the forcing required to maintain a

Re_θ	Method	Domain size $(L_x \times L_y \times L_z)/\theta$	Grid $(n_x \times n_y \times n_z)$	ΔT^+	T_f^+	Total cost (Core-hour)
1000	DNS	$40 \times 30 \times 15$	$192 \times 257 \times 128$	0.0214	4285	1280
2000	DNS	$40 \times 30 \times 15$	$352 \times 465 \times 224$	0.0177	7079	10752
4060	ILES	$60 \times 30 \times 15$	$320 \times 305 \times 128$	0.0482	12958	3584
6500	ILES	$80 \times 30 \times 15$	$640 \times 449 \times 224$	0.0407	20347	31360
8300	ILES	$120 \times 30 \times 15$	$1216 \times 545 \times 272$	0.0393	27538	163840

Table 1. Simulation details for the DNS and ILES of (4.1).

unity value of momentum thickness in ILES. For simplicity, a gain value of $k = 1$ is used throughout this paper.

4.2. *Computational domains, data collection and computational cost*

The DNS are performed at $Re_\theta = 1000, 2000$ and the ILES at $Re_\theta = 4060, 6500, 8300$. These Reynolds numbers have been selected in order to allow for a direct comparison with published numerical data of a spatially evolving turbulent boundary layer. The spatial discretisation, temporal discretisation and computational cost of each simulation run are given in table 1. With increasing Reynolds number it is necessary to use both a longer temporal window and a larger domain in the streamwise direction to obtain converged statistics. For example, L_x is chosen to be $40/\theta$ for $Re_\theta = 1000$ and is increased by a factor of three for $Re_\theta = 8300$.

The flow statistics are computed by first performing a space/time average to obtain the mean streamwise velocity profile $U(y)$ and, subsequently, the wall shear stress $\tau_w = \nu U'(0)$ and friction velocity $U_\tau := \sqrt{\tau_w/\rho} = \sqrt{\tau_w}$. Using $l_* = \nu/U_\tau$ as a length scale and $t_* = l_*/U_\tau$ as a time scale, all variables can be expressed in wall units, e.g. $u^+ = U/U_\tau$, $y^+ = y/l_*$, and $t^+ = t/t_*$. In addition to the displacement thickness δ^* and momentum thickness θ, we will also consider the 'shape factor' $H_{12} := \delta^*/\theta$, and the wake parameter

$$C_{wake} = \int_0^\infty \left(U_\infty^+ - U^+ \right) d(y/\delta), \tag{4.5}$$

introduced by Coles (1956), where δ is the boundary layer thickness defined in terms of 99 % of the free-stream velocity.

The mean values of all flow statistics reported in subsequent sections are collected after the flow was observed to have transitioned to a statistically steady state. For the five Reynolds numbers considered in table 1, this was deemed to occur at non-dimensional times $t_0^+ = 1976, 3418, 7534, 12\,208$ and $16\,511$, ordered in terms of increasing Re_θ. Each flow statistic was then averaged over a window $t^+ \in [t_0^+, T_f^+]$, respectively (see table 1), in order of increasing Re_θ. To describe statistical convergence, suppose that $g(t)$ is a given time-dependent flow property of interest, and $\bar{g}$ is its average over the window $[t_0^+, T_f^+]$. Letting

$$G(t^+) = \frac{1}{t^+ - t_0^+} \int_{t_0^+}^{t^+} g(s)\mathrm{d}s, \tag{4.6}$$

Case	Method	Δx^+	Δy_{min}^+	Δz^+	Re_θ	Marker	Line patterns
Present	DNS	10	0.5	5.5	—	□	Solid(-)
Present	ILES	30	1.5	16.5	—	□	Solid(-)
Schlatter & Orlu (2010)	DNS	18	0.35	9.6	4300	○	Dashed(- -)
Eitel-Amor *et al.* (2014)	LES	18	0.06	8	8300	○	Dashed(- -)
Sillero *et al.* (2013)	DNS	7	0.32	4.07	6500	▽	Dashdotted ($-\cdot$)

Table 2. The DNS and LES grid resolutions, and figure formatting conventions.

be the moving average of g, we define the maximum percentage deviation of the moving average from the reported mean over the final half of the averaging window by

$$E = \max \left\{ 100\,\% \cdot \left| \frac{G(t^+) - \bar{g}}{\bar{g}} \right| : \frac{t_0^+ + T_f^+}{2} \leqslant t^+ \leqslant T_f^+ \right\}. \tag{4.7}$$

The maximum value of E for any of the flow statistics δ^*, U_τ, f, C_{wake} that we report subsequently in table 3 is, 1.2 %, 0.9 %, 0.9 %, 1.1 % and 1.5 %, respectively, for the five cases considered in order of increasing Re_θ.

Finally, we note that there are significant differences in computational cost, detailed in 1, of the proposed numerical scheme in comparison with that of the highlighted reference studies listed in table 2. The DNS of Sillero *et al.* (2013), achieving a maximum Reynolds number of $Re = 6500$, is computationally expensive, and required 45 million core hours while using a large number of cores (32 768). The LES of Eitel-Amor *et al.* (2014), achieving a maximum Reynolds number of $Re_\theta = 8300$, used only around 1 million core hours and 4096 cores. In this study, we sought a balance between computational cost and efficiency. At the highest Reynolds number considered in this study, $Re_\theta = 8300$, the proposed numerical scheme used 1 60 384 core hours on 8192 cores, a sixfold reduction compared with the LES of Eitel-Amor *et al.* (2014).

5. Results

In § 5.1 the DNS implementation of the numerical method proposed in this paper is validated against the DNS of Biau (2023) at $Re_\theta = 1000, 2000$. Subsequently, in § 5.2, an ILES implementation of the periodic boundary layer equations (4.1) at $Re_\theta = 4060, 6500, 8300$ is compared with reference data from the DNS of Schlatter & Orlu (2010) and Sillero *et al.* (2013), and with the LES of Eitel-Amor *et al.* (2014). The reference data were obtained for spatially evolving turbulent boundary layers.

A common colour scheme is used throughout § 5 to indicate data from simulations at different Reynolds numbers: (——) black for $Re_\theta = 1000$; (——) purple for $Re_\theta = 2000$; (——) blue for $Re_\theta = 4060$; (——) red for $Re_\theta = 6500$; and (——) green for $Re_\theta = 8300$.

Results using the method presented in this paper are shown with solid lines (······), and those from an implementation of the method of Biau (2023) using `Xcompact3d` are shown with dotted lines ($\times$). Data extracted directly from Biau (2023) are shown with ($\times$); those from the DNS of Schlatter & Orlu (2010) at $Re_\theta = 1000, 2000, 4060$ are shown with circles (○), while data from the DNS of Sillero *et al.* (2013) at 6500 are shown with closed triangles (▼). The LES of Eitel-Amor *et al.* (2014) at $Re_\theta = 6500, 8300$ are also shown with circles (▼), since on all subsequent figures these data are always visually distinguishable from those of Schlatter & Orlu (2010).

1020 A6-18

Table 2 also reports the grid resolutions in wall units between the present study and the reference works. For DNS, achieving accurate statistical results requires capturing a wide range of scales, e.g. from the boundary layer thickness to the Kolmogorov length scale. Proper grid resolution is essential for this purpose. While it is ideal to fully resolve both scales, previous DNS studies have demonstrated that good agreement with experiments can still be achieved even when the Kolmogorov length scale remains partially under-resolved. This trade-off between accuracy and computational cost is noteworthy. Moin & Mahesh (1998) proposed one possible set of grid resolutions, expressed in wall units as ($\Delta x^+ = 14.3$, $\Delta y^+ = 0.33$, $\Delta z^+ = 4.8$), which seeks to strike this balance. Of the considered reference studies, the DNS of Sillero *et al.* (2013) used a grid resolution within the same range for both normal and spanwise directions, while Schlatter & Orlu (2010) used a fine spatial resolution in the normal direction, and a coarser grid in the streamwise and spanwise directions. The DNS performed in this paper have similar mesh resolutions to those in the reference data. For the ILES, following the work of (Mahfoze & Laizet 2021), the spatial resolution is more or less three times larger per spatial direction than in the DNS, while keeping a fine mesh close to the wall in the normal direction.

Finally, we note that the reference data are obtained for a spatially evolving turbulent boundary layer, and the reported wall units are typically scaled based on the Re_θ close to the end of the computational domain. In contrast, for the periodic turbulent simulations conducted here, Re_θ is constant throughout the simulation, which is advantageous since it allows a targeted choice of mesh resolution to be made *a priori*.

5.1. *Validation against Biau (2023)*

We perform DNS by solving (4.1) with $\Gamma = 0$ and with the forcing amplitude f, given by (4.2), at $Re_\theta = 1000$, 2000. Data are compared with those extracted from Biau (2023) (obtained with a different flow solver), and with a separate implementation of Biau's numerical scheme (in which $\theta = 1$ is imposed at each time step via the iterative solution of an optimisation problem).

The temporal evolution of f, θ, δ^* and u_τ is shown in figure 2. The instantaneous friction velocity u_τ is defined in terms of the wall-normal derivative of the streamwise- and spanwise-averaged wall-normal velocity

$$u_\tau = \nu \frac{\partial U}{\partial y}(0, t). \tag{5.1}$$

For the two implementations of Biau's method, the momentum thickness satisfies $\theta = 1$ at all times. The present method has the same behaviour as the method initially designed by Biau, apart from a small initial transient corresponding to an exponential convergence of the error $e_\theta \to 0$. For all three methods (Biau's original method and solver; Biau's original method with Xcompact3d; and the present method with Xcompact3d), f approaches a statistically steady state with mean values of approximately 0.0012 for $Re_\theta = 1000$, and 0.0014 for $Re_\theta = 2000$. This confirms the veracity the analytical expression for the asymptotic value of the forcing term (2.13) in this case.

It is interesting to observe that, for all methods, the displacement thickness δ^*, whose value is not prescribed, also converges to a constant. This constant is observed to decrease with increasing Reynolds number, implying a corresponding decrease in shape factor $H_{12} = \delta^*/\theta$, which is in line with the observations presented in Schlatter & Orlu (2010). Similarly, the friction velocity u_τ also decreases with increasing Reynolds number. Overall, the relative error between any of the three methods for any of the flow statistics
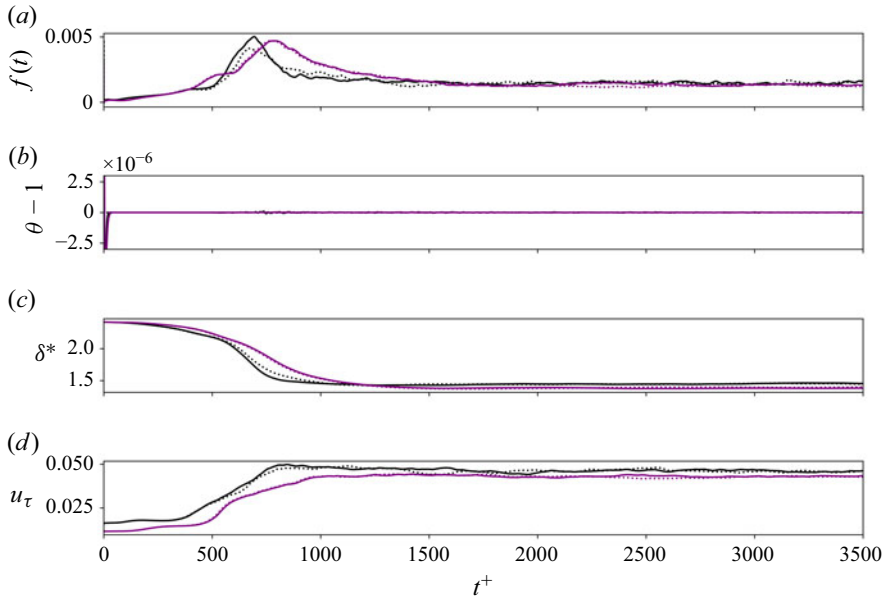
Figure 2. Temporal variation of the forcing amplitude f, momentum thickness θ, displacement thickness δ^* and friction velocity u_τ. Data from the present DNS using f_{DNS} are shown with solid lines (——$Re_\theta = 1000$; ——$Re_\theta = 2000$) and from implementation of Biau's method in `Xcompact3d` with dotted lines (······$Re_\theta = 1000$; ······$Re_\theta = 2000$).

U_τ, δ, δ^*, θ, H_{12}, C_f and C_{wake} does not deviate by more than 1 %, indicating excellent agreement between the current implementation and with the data presented in Biau (2023).

Figure 3 shows the mean stream wise velocity u^+ and root-mean-square (r.m.s.) velocity and pressure profiles obtained from the three methods. The implementation of Biau's method in `Xcompact3d` compares very well with the present method. Both exhibit small, but noticeable, differences from data extracted directly from Biau (2023) which are most prominent in u^+ and p_{rms}^+ in the outer layer for $Re_\theta = 1000$. These discrepancies are lower at $Re_\theta = 2000$ and it is important to note that at this Reynolds number the implementation of the present method in `Xcompact3d` is shown in §5.2.2 to compare very well with reference DNS data from spatially evolving boundary layers.

5.2. *Comparison against spatially evolving turbulent boundary layer data*

5.2.1. *Statistical quantities*

Table 3 presents some key statistics for the turbulent boundary layer flows simulated with the present method and those of the selected reference data for spatially evolving turbulent boundary layers. It should be emphasised that for the present method the fixed control parameter is Re_θ, while the other reported statistics are emergent properties of the flow. Furthermore, throughout this section the friction Reynolds number is defined in terms of the 99 % boundary layer thickness via $Re_\tau = U_\tau \delta / \nu$.

The wake statistics for the present method compare very well with the reference data, with H_{12}, Re_{δ^*} and U_τ not deviating by more than 2 % from any of the corresponding reference data values, for any of the considered Reynolds numbers Re_θ. The skin-friction coefficient C_f also compares very well with the reference data, with a maximum deviation of only 3.3 % from the results of Sillero *et al.* (2013) at $Re_\theta = 6500$.
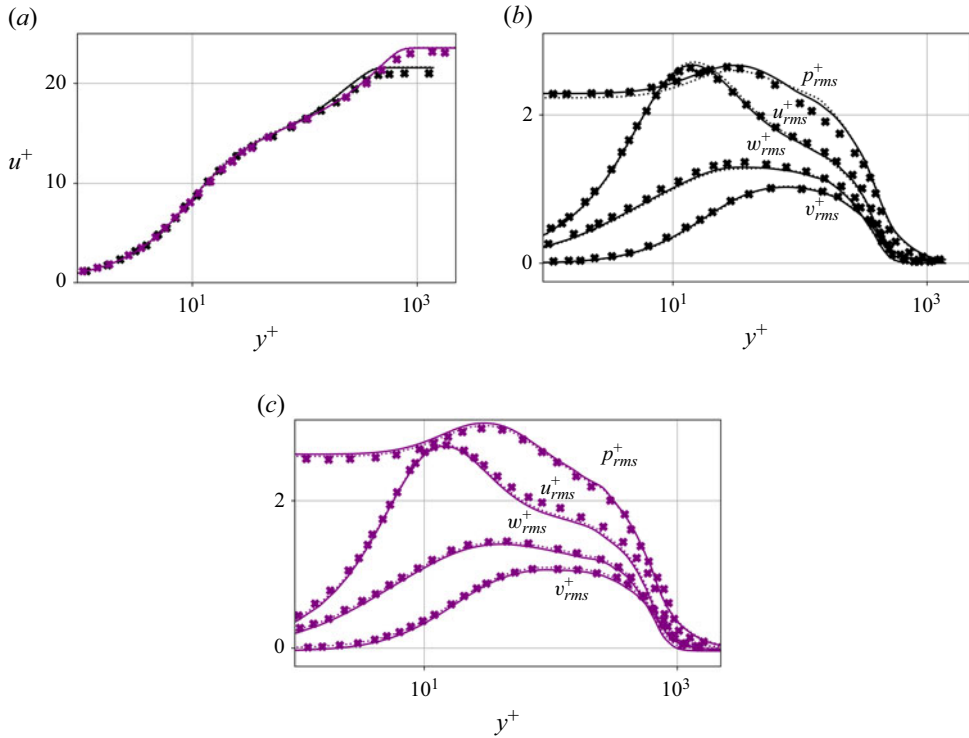
1020 A6-20

Figure 3. A comparison of DNS of the current method with that of Biau (2023): (*a*) mean streamwise velocity u^+; (*b*) r.m.s. velocities and pressures at $Re_\theta = 1000$; (*c*) r.m.s. velocities and pressures at $Re_\theta = 2000$. Data from Biau (2023) are shown with markers ($\times$ $Re_\theta = 1000$; $\times$ $Re_\theta = 2000$), from the present DNS using f_{DNS} with solid lines (——$Re_\theta = 1000$; ——$Re_\theta = 2000$) and from the implementation of Biau's method in Xcompact3d with dotted lines (······$Re_\theta = 1000$; ······$Re_\theta = 2000$).

Case	Re_θ	Re_τ	Re_{δ^*}	U_τ	H_{12}	C_f	$f(t)$	C_{wake}	δ^*
Present	1000	398	1448	0.0463	1.448	0.00429	0.00141	3.578	1.448
Schlatter & Orlu (2010)	1006	359	1459	0.0462	1.445	0.00426	—	4.062	1.451
Sillero *et al.* (2013)	1100	445	1585	0.0462	1.434	0.00426	—	3.586	1.434
Present	2000	712	2806	0.0421	1.403	0.00359	0.00121	3.938	1.403
Schlatter & Orlu (2010)	2000	671	2827	0.0421	1.414	0.00353	—	4.214	1.414
Sillero *et al.* (2013)	1968	690	2780	0.0422	1.416	0.00356	—	3.984	1.418
Present	4060	1315	5614	0.0385	1.383	0.00298	0.00102	4.269	1.383
Schlatter & Orlu (2010)	4061	1271	5633	0.0385	1.387	0.00297	—	4.431	1.387
Sillero *et al.* (2013)	4000	1306	5589	0.0390	1.377	0.00304	—	4.324	1.375
Present	6500	2141	8749	0.0373	1.346	0.00279	0.00097	4.085	1.346
Eitel-Amor *et al.* (2014)	6500	1972	8886	0.0368	1.367	0.00273	—	4.494	1.364
Sillero *et al.* (2013)	6500	1989	8879	0.0368	1.363	0.00270	—	4.492	1.363
Present	8300	2763	10 987	0.0368	1.324	0.00272	0.00095	3.976	1.324
Eitel-Amor *et al.* (2014)	8300	2557	11 192	0.0364	1.348	0.00265	—	4.464	1.352

Table 3. A comparison of flow statistics between periodic boundary layer and spatially evolving boundary layer simulations.
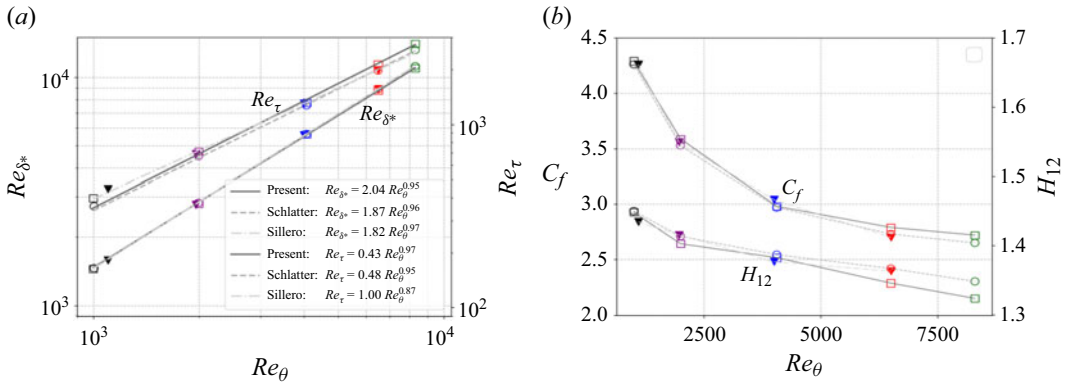
Figure 4. The scaling of (*a*) Re_τ and $Re_{\delta*}$; and (*b*) C_f and H_{12} with Re_θ. The markers indicate: (○) for both DNS data from Schlatter & Orlu (2010) and LES data from Eitel-Amor *et al.* (2014); (▼) for DNS data from Sillero *et al.* (2013); and (□) data from the present method.

Slightly larger discrepancies are observed for the friction Reynolds number Re_τ and the wake coefficient C_{wake}. These have maximum deviations of 10.8 % and 11.9 %, respectively, from the DNS of Schlatter & Orlu (2010) at $Re_\theta = 1000$, although these deviations decrease with Reynolds number and are below 4 % for $Re_\theta = 4060$. The larger discrepancies for Re_τ and C_{wake} can be explained by the fact that both are defined in terms of the 99 % boundary layer thickness δ, as opposed to H_{12}, $Re_{\delta*}$, which are defined using the displacement thickness δ^*. Since δ is a pointwise measure of the boundary layer thickness, this is a less robust statistic than the integral quantity δ^*. This is important, given that the forcing $f \sim y(\partial u/\partial y)$ required to maintain the momentum thickness is of largest magnitude away from the wall.

The above observations are confirmed by figure 4 which shows excellent agreement between the present method and the reference data in terms of the scaling of displacement Reynolds number (in figure 4*a*), and the skin-friction coefficient and shape factor (in figure 4*b*) with Re_θ. Slightly larger deviations for the reference data can be observed in figure 4(*a*) in terms of the scaling of Re_τ with Re_θ. Despite this, numerical fits (shown in the legend of figure 4*a*) to the data reveal near-linear scalings of Re_τ and $Re_{\delta*}$ with the control parameter Re_θ, namely

$$Re_\tau \approx \alpha_1 Re_\theta^{\beta_1} \quad \text{and} \quad Re_{\delta*} \approx \alpha_2 Re_\theta^{\beta_2}, \tag{5.2}$$

for prefactors in the ranges $0.41 \leqslant \alpha_1 \leqslant 1$ and $1.82 \leqslant \alpha_2 \leqslant 2.84$ and scaling exponents in the ranges $0.87 \leqslant \beta_1 \leqslant 0.97$ and $0.95 \leqslant \beta_2 \leqslant 0.97$. The smaller range of scaling exponents for β_2 again confirms that $Re_{\delta*}$ is a more robust statistic than Re_τ.

These numerical fits are consistent with the theoretical scaling laws proven in § 3, which state that the scaling exponents cannot exceed $\beta = 1$. It is still an open theoretical question whether the small observed deviations of the scaling exponents β_1, β_2 from this value arise due to a logarithmic term in the true scaling law for the skin friction in turbulent boundary layers.

5.2.2. *Velocity profiles, fluctuating statistics and turbulent kinetic energy budgets*
Figure 5(*a*) shows the mean velocity profile u^+ in comparison with the reference data from spatially evolving boundary layer simulations at comparable Reynolds numbers. Excellent agreement can be observed in the inner layer, with only small deviations in the wake region. In the linear and logarithmic regions, a grey line shows the fit $\kappa^{-1} \ln y^+ + B$
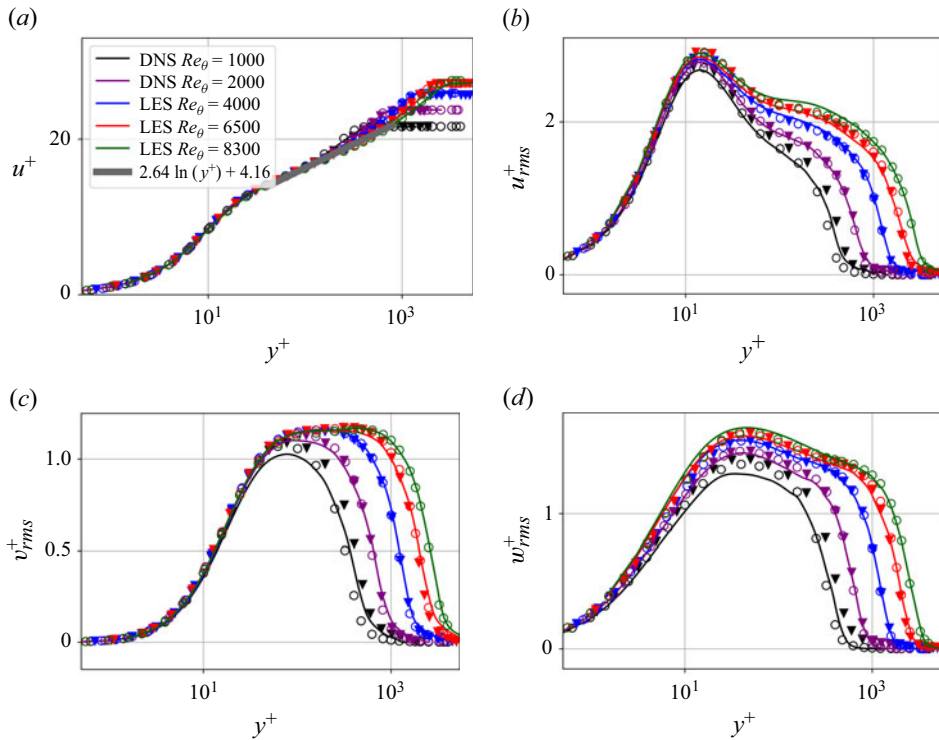
Figure 5. Profiles of (*a*) u^+; (*b*) u^+_{rms}; (*c*) v^+_{rms}; and (*d*) w^+_{rms}. Reference data are shown with markers: (○) for both the DNS of Schlatter & Orlu (2010) and the LES of Eitel-Amor *et al.* (2014); (▼) for the DNS of Sillero *et al.* (2013). Results with the present method are shown with solid lines. The colour convention is explained in § 5.

with $\kappa = 0.379$ and $B = 4.161$ to the present data, which is in good agreement with that presented in Eitel-Amor *et al.* (2014). As Re_θ increases, the asymptotic value of u^+ in the wake region increases from $u^+ = 21.60$ at $Re_\theta = 1000$ to $u^+ = 27.13$ at $Re_\theta = 8300$, indicated by the arrow in figure 5(*a*), with very good agreement between the reference data and the present method.

Figure 5 (*b–d*) show profiles of r.m.s. velocity fluctuations. Again, these reveal a good agreement between data from periodic and spatially evolving simulations. The peak values of the streamwise velocity fluctuations u^+_{rms} are observed to lie consistently in the buffer layer at $y^+ \approx 14$, which agrees well with the value of $y^+ \approx 15$ reported by both Smits *et al.* (2021) and Devenport & Lowe (2022). Following this peak value u^+_{rms} decreases, with the rate of decrease slowing in the overlap region near $y^+ \approx 100$. Here, the gradient $\partial u^+_{rms}/\partial y^+$ is observed to increase with Re_θ, with data from the highest considered Reynolds number $Re_\theta = 8300$ exhibiting a plateau consistent with the experimental observations of Devenport & Lowe (2022) for spatially evolving boundary layers.

Regarding peak values of the r.m.s. velocities, Smits *et al.* (2021) reported that the peak value of the squared r.m.s. streamwise velocity, denoted u^{2+}_{rms}, was observed to lie on the line $3.54 + 0.646 \ln(Re_\tau)$ for friction Reynolds numbers in the range $6123 \leqslant Re_\tau \leqslant 19680$. Although our studies are at lower Reynolds numbers, we observe a similar relationship of $3.88 + 0.56 \ln(Re_\tau)$. This compares well with analogous fits to the combined data of Schlatter & Orlu (2010), Eitel-Amor *et al.* (2014) and to the data of Sillero *et al.* (2013),

	u_{rms}^{2+}			v_{rms}^{2+}			w_{rms}^{2+}		
	α	β	R^2	α	β	R^2	α	β	R^2
Present	0.56	3.88	0.973	0.1	0.57	0.875	0.4	−0.51	0.982
Schlatter & Orlu (2010) and Eitel-Amor *et al.* (2014)	0.58	3.96	0.996	0.1	0.6	0.918	0.37	−0.26	0.996
Sillero *et al.* (2013)	0.71	3.15	0.994	0.12	0.48	0.973	0.38	−0.3	0.999

Table 4. Linear regression coefficients α, β and correlation statistics R^2 for fits of the peak value of the squared r.m.s. velocity, u_{rms}^{2+}, v_{rms}^{2+} and w_{rms}^{2+} to the line $\alpha \ln (Re_\tau) + \beta$. Fits are reported to data from the present study; the combined data of Schlatter & Orlu (2010), Eitel-Amor *et al.* (2014); and the data of Sillero *et al.* (2013).

revealing relationships of $3.96 + 0.58 \ln(Re_\tau)$ and $3.15 + 0.71 \ln(Re_\tau)$, respectively. We note that, for this analysis, the data of Schlatter & Orlu (2010) and Eitel-Amor *et al.* (2014), which were produced by the same group and the same code, were combined to achieve a wider range of Reynolds numbers. Table 4 also shows that the location of the peak values of v_{rms}^{2+} and w_{rms}^{2+} also lie on the lines of the form $\alpha \ln (Re_\tau) + \beta$ with a good degree of confidence, and that there is good agreement between the present results and data from the considered reference studies. For clarity, we emphasise that the logarithmic dependence of the peak values of r.m.s. velocities discussed here gives no information on whether the quantity $\overline{E_v}$, discussed in § 3 and Corollary 1, exhibits the logarithmic growth required to bring our theoretical results into full agreement with empirical observations. The reason is that $\overline{E_v}$ is defined as an integral quantity over the whole domain, as opposed to the pointwise observations regarding peak values discussed in this section.

Regarding differences between periodic boundary layers and the spatially evolving reference data, the most prominent are in the case $Re_\theta = 1000$ where differences are apparent in all three r.m.s. velocity profiles, as well as in the Reynolds shear stress and r.m.s. pressure profiles shown in figure 6. However, it can be seen in figures 5 and 6 that these differences decrease significantly with Re_θ, a finding that is consistent with the analysis of Kozul *et al.* (2016) for temporal, periodic, boundary layers. A slight deviation is observed between the u_{rms}^+ profile obtained in the present study and that of Eitel-Amor *et al.* (2014) for $Re_\theta = 8300$. A possible cause of this discrepancy is that in this simulation of a spatially evolving boundary layer, the spatial location for the statistics for $Re_\theta = 8300$ is very close to the outlet of the computational domain, with Eitel-Amor *et al.* (2014) only technically reporting results on u^+ up to $Re_\theta = 7500$. At such a location, the outlet boundary conditions can cause spurious, non-physical behaviour. Thus, while we believe it is useful to consider the data from Eitel-Amor *et al.* (2014) at $Re_\theta = 8300$ for comparison, they should be treated with appropriate caution. It was reported in Fernholz & Finley (1996) that the peak location of the Reynolds shear stress is proportional to $\sqrt{Re_\tau}$. Our observations support this, revealing a strong correlation ($R^2 = 0.984$) of this peak value with the line $2.24\sqrt{Re_\tau} + 0.97$. A similar analysis using the combined data from Schlatter & Orlu (2010), Sillero *et al.* (2013) and Eitel-Amor *et al.* (2014), yields fits of $2.48\sqrt{Re_\tau} - 0.1$ ($R^2 = 0.847$) and of $2.99\sqrt{Re_\tau} + 19.35$ ($R^2 = 0.951$), respectively, and show proportionality constants in good agreement with the data using the present method. Finally, we note that figure 6 shows discrepancies in p_{rms}^+ near the wall between the present method and the reference data, which can be attributed to the coarser near-wall grid resolution employed in this study (see table 2).

Figure 7 shows the mean turbulent kinetic energy budget for $Re_\theta = 1000$ and 6500. It can be seen that the largest difference between periodic and spatially evolving boundary layers are obtained for the lowest Reynolds number. In particular, the production, dissipation and
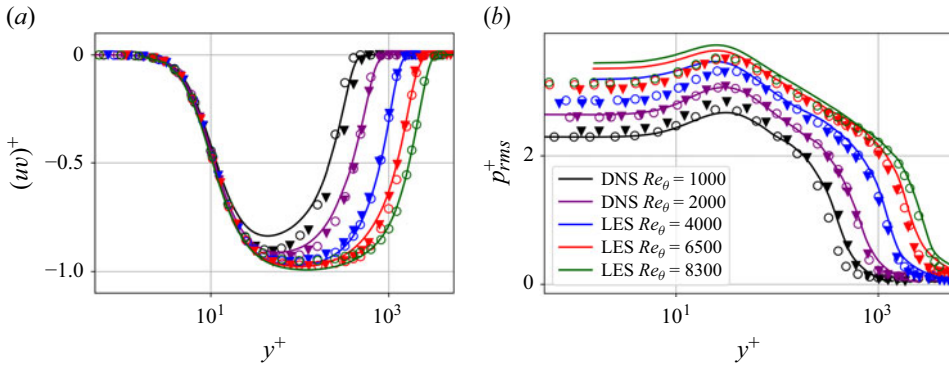
Figure 6. (*a*) Mean Reynolds shear stress; and (*b*) r.m.s. pressure profiles. Reference data are shown with markers: (○) for both the DNS of Schlatter & Orlu (2010) and the LES of Eitel-Amor *et al.* (2014); (▼) for the DNS of Sillero *et al.* (2013). Results with the present method are shown with solid lines.
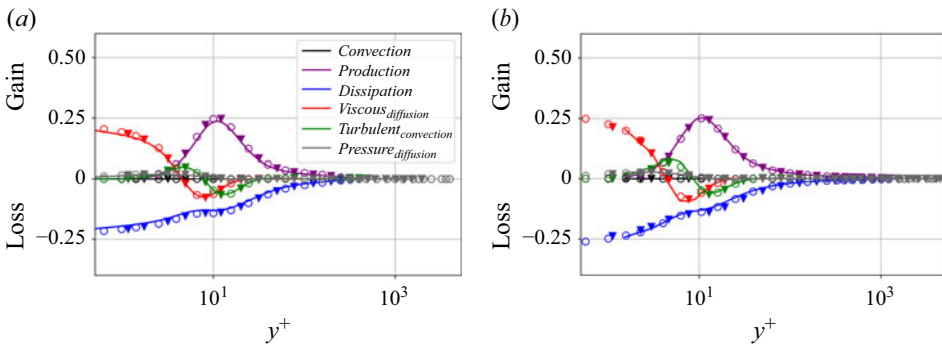

Figure 7. Turbulent kinetic energy budgets for (*a*) $Re_\theta = 1000$ and (*b*) $Re_\theta = 6500$. Reference data are shown with markers: (○) for both the DNS of Schlatter & Orlu (2010) and the LES of Eitel-Amor *et al.* (2014); (▼) for the DNS of Sillero *et al.* (2013). Results with the present method are shown with solid lines.

viscous diffusion components of the budget have consistently lower magnitudes in the periodic case when compared with the spatially evolving case. For the highest Reynolds number in the figure the present energy budget is in excellent agreement with the reference data.

5.2.3. *Vorticity profiles and instantaneous visualisations*

Figure 8 shows the profiles of the r.m.s. vorticity components. Overall, there is very good agreement between the present method and the reference data, in terms of the locations of minimum and maximum r.m.s. vorticity, as well as the general profile shapes. The peak location of $\omega_{y_{rms}}$ is in the buffer layer at $y^+ \approx 13$, which is consistent with the results of Schlatter & Orlu (2010), Sillero *et al.* (2013) and Eitel-Amor *et al.* (2014).

Finally, we use the Q-criterion to visualise the vortical structures generated in our periodic turbulent boundary layer flows. The Q-criterion can be used to measure the local balance of rotation and strain rate, being defined by $Q = 1/2(\|\Omega\|_F^2 - \|S\|_F^2)$, where $S = 1/2(\partial u_i/\partial x_j + \partial u_j/\partial x_i)$ is the stain rate tensor, $\Omega = 1/2(\partial u_i/\partial x_j - \partial u_j/\partial x_i)$ is the vorticity tensor and $\|\cdot\|_F$ is the Frobenius norm. The Q-criterion is normalised using wall units as $Q^+ = Q(t^+)^{-2} = Q\nu^2(U_\tau)^{-4}$. The normalised Q-criterion plots, which show contours at the values of $Q^+ = 0.01, 0.004$ at the Reynolds numbers $Re_\theta = 1000, 6500,$
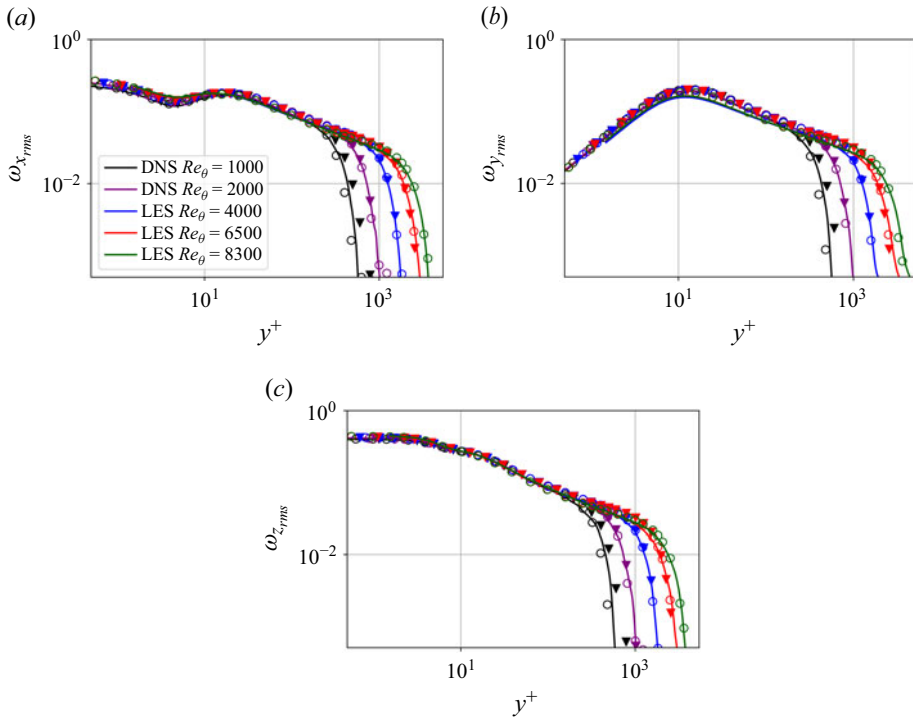
Figure 8. Profiles of the r.m.s. vorticity components (a) $\omega_{x_{rms}}$; (b) $\omega_{y_{rms}}$; and (c) $\omega_{z_{rms}}$, for $Re_\theta = 1000$ to 8300. Reference data are shown with markers: (○) for both the DNS of Schlatter & Orlu (2010) and the LES of Eitel-Amor *et al.* (2014); (▼) for the DNS of Sillero *et al.* (2013). Results with the present method are shown with solid lines.

respectively, are presented in figure 9. As expected, a wider range of turbulent scales can be observed for the DNS than the ILES, with finer vortices apparent as the Reynolds number is increased. It should be noted that the ILES does not produce spurious oscillations, suggesting that the numerical dissipation is acting properly. The shape and structure of the vortices (mainly elongated structures in the streamwise direction, slightly inclined up with respect to the wall) is similar to the ones observed in spatially evolving turbulent boundary layers. It is clear that the periodic boundary layer model considered in this paper appears to capture the expected features of canonical turbulent boundary layers across a range of Reynolds numbers.

6. Conclusions

In this paper we have performed a rigorous analytical study of the periodic boundary layer equations proposed by Biau (2023), in which a body force is used to maintain the boundary layer thickness of the flow. It is shown that an explicit formula can be obtained for the amplitude of this body force as a function of the flow velocity field. This enabled a PDE to be identified for the flow, as opposed to the implicit definition given by Biau (2023).

The explicit form of the PDE was important for two reasons. First, it allowed an application of the 'background field' method of Constantin–Doering–Hopf, and we proved that the skin-friction coefficient of the periodic boundary layer flow was upper bounded
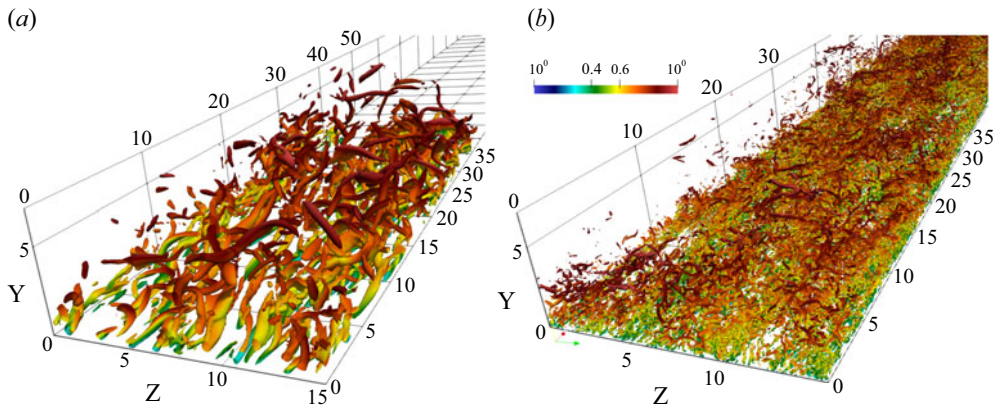
Figure 9. Contours of constant Q^+ for selected snapshots of a periodic turbulent boundary layer at (a) $Re_\theta = 1000$, $Q^+ = 0.01$; (b) $Re_\theta = 6500$, $Q^+ = 0.004$. The colour bar indicates non-dimensional streamwise velocity u. Each panel shows a section of the respective spatial domains described in table 1.

by an absolute constant. Future work will investigate wither this constant can be reduced by implementing computationally an optimal version of the proof presented in this paper.

The second implication of our explicit formula for the forcing amplitude was that it allowed the construction of a simple numerical scheme for simulating turbulent boundary layers on periodic domains which can be used with both DNS and ILES approaches. Validation of this scheme was presented, with results shown to closely match those from Biau (2023), but also with data from spatially evolving turbulent boundary layers up to $Re_\theta = 8300$. It was observed that the similarity between the two classes of flow was greater at higher Reynolds number. This is important, since periodic turbulent boundary layer simulations can be performed at a lower computational cost than simulations of spatially evolving boundary layers. For example, the ILES of a periodic boundary layer flow at $Re_\theta = 8300$ performed in this study is nearly 300 times cheaper than the DNS of Sillero *et al.* (2013), and about 6 times cheaper than the LES of Eitel-Amor *et al.* (2014) for spatially evolving boundary layers at comparable Reynolds numbers.

In conclusion, this paper presented a detailed theoretical and numerical study of turbulent boundary layer flows and investigated their statistical similarity with canonical spatially evolving boundary layers. Further investigations at higher Reynolds numbers and exploration of more complex flow scenarios are warranted to fully explore our findings.

Appendix A.

In this section we provide detailed proofs of Lemma 1, Lemma 2 and the energy equation (3.4).

A.1. *Proof of (2.2) and Lemma 1*

Proof. By taking the streamwise and spanwise average of (2.8), it can be shown that

$$\frac{\partial U}{\partial t} + \frac{\partial}{\partial y}\langle uv \rangle = \frac{1}{Re}\frac{\partial^2 U}{\partial y^2} + f(t)y\frac{\partial U}{\partial y}. \tag{A1}$$

Using the boundary conditions, it follows that

$$\frac{\mathrm{d}\delta^*}{\mathrm{d}t} = -\int_0^\infty \frac{\partial U}{\partial t}\mathrm{d}y = \frac{1}{Re}\frac{\partial U}{\partial y}(0,t) - f(t)\int_0^\infty y\frac{\partial U}{\partial y}\mathrm{d}y. \tag{A2}$$

We next apply integration by parts to the final term and use the assumption that $y(1 - u(y)) \to 0$ as $y \to \infty$ to obtain

$$\int_0^\infty y\frac{\partial U}{\partial y}\mathrm{d}y = \int_0^\infty y\frac{\partial(U-1)}{\partial y}\mathrm{d}y = \left[y(U-1)\right]_{y=0}^\infty + \int_0^\infty (1-U)\mathrm{d}y = \delta^*. \tag{A3}$$

Hence,

$$\frac{\mathrm{d}\delta^*}{\mathrm{d}t} = -f(t)\delta^*(t) + \frac{1}{Re}\frac{\partial U}{\partial y}(0,t). \tag{A4}$$

Letting $e_\delta(t) = 1 - \delta^*(t)$ and using the control law

$$f(t) = \frac{-ke_\delta(t) + \frac{1}{Re}\frac{\partial U}{\partial y}}{\delta^*(t)}, \tag{A5}$$

it follows that $\dot{e}_\delta = -ke_\delta$. Hence, $e_\delta(t) \to 0$ as $t \to \infty$. $\qquad\square$

A.2. *Proof of (2.9) and Lemma 2*

Proof. Using (A1)

$$\begin{aligned}
\frac{\mathrm{d}\theta}{\mathrm{d}t} &= \int_0^\infty \frac{\partial U}{\partial t} - 2U\frac{\partial U}{\partial t}\mathrm{d}y \\
&= -\frac{\mathrm{d}\delta^*}{\mathrm{d}t} + 2\int_0^\infty U\frac{\partial\langle uv\rangle}{\partial y} - \frac{2}{Re}\int_0^\infty U\frac{\partial^2 U}{\partial y^2}\mathrm{d}y - 2f(t)\int_0^\infty yU\frac{\partial U}{\partial y}\mathrm{d}y \\
&= f(t)\delta^*(t) - \frac{1}{Re}\frac{\partial U}{\partial y}(0,t) \\
&\quad - 2\int_0^\infty \frac{\partial U}{\partial y}\langle uv\rangle\mathrm{d}y + \frac{2}{Re}\int_0^\infty \left(\frac{\partial U}{\partial y}\right)^2\mathrm{d}y - 2f(t)\int_0^\infty yU\frac{\partial U}{\partial y}\mathrm{d}y, \tag{A6}
\end{aligned}$$

where in the final line, we have used integration by parts, the boundary conditions (1.5), and the identity (A4). To evaluate the final term, we again use integration by parts and the assumption that $y(1 - U(y)) \to 0$ as $y \to \infty$ to obtain

$$\begin{aligned}
\int_0^\infty yU\frac{\partial U}{\partial y}\mathrm{d}y &= \int_0^\infty yU\frac{\partial(U-1)}{\partial y}\mathrm{d}y \\
&= \left[yU(U-1)\right]_{y=0}^{y=\infty} - \int_0^\infty U(U-1)\mathrm{d}y - \int_0^\infty y(U-1)\frac{\partial U}{\partial y}\mathrm{d}y \\
\text{(by (A3))} &= \theta + \delta - \int_0^\infty yU\frac{\partial U}{\partial y}\mathrm{d}y. \tag{A7}
\end{aligned}$$

Combining (A6) and (A7) gives

$$\frac{d\theta}{dt} = -f(t)\theta(t) - \frac{1}{Re}\frac{\partial U}{\partial y}(0, t) - 2\int_0^\infty \frac{\partial U}{\partial y}\langle uv\rangle dy + \frac{2}{Re}\int_0^\infty \left(\frac{\partial U}{\partial y}\right)^2 dy. \quad (A8)$$

Hence, if $e_\theta(t) = 1 - \theta(t)$ and $f(t)$ is given by (2.12), it follows that

$$\frac{de_\theta}{dt} = -ke_\theta(t), \quad (A9)$$

and, hence, $e_\theta(t) \to 0$ as $t \to \infty$. □

A.3. *Proof of the energy identity (3.4)*

Proof. After taking the dot product of (1.4) with $\boldsymbol{u} - \boldsymbol{e}_x$, integrating over Ω, and using incompressibility, the boundary conditions, and (1.8) gives

$$\frac{1}{2}\frac{d}{dt}\|\boldsymbol{u} - \boldsymbol{e}_x\|^2 + \frac{1}{Re}\|\nabla\boldsymbol{u}\|^2 = f(t)\int_\Omega y(\boldsymbol{u} - \boldsymbol{e}_x)\cdot\frac{\partial\boldsymbol{u}}{\partial y}dx + \frac{1}{2}C_f(t), \quad (A10)$$

where the final two terms in the above equation arise from

$$\frac{1}{Re}\int_\Omega (\boldsymbol{u} - \boldsymbol{e}_x)\cdot\Delta\boldsymbol{u}dx = \frac{1}{Re}\|\nabla\boldsymbol{u}\|^2 - \frac{1}{Re}\int_\Omega \left(\frac{\partial^2 u}{\partial x^2} + \frac{\partial^2 u}{\partial y^2} + \frac{\partial^2 u}{\partial z^2}\right)dx$$

$$\text{(using periodic b.c.s)} = \frac{1}{Re}\|\nabla\boldsymbol{u}\|^2 - \frac{1}{Re}\int_\Omega \frac{\partial^2 u}{\partial y^2}dx$$

$$\text{(by (3.3))} = \frac{1}{Re}\|\nabla\boldsymbol{u}\|^2 + \frac{1}{Re}\frac{\partial U}{\partial y}(0, t)$$

$$= \frac{1}{Re}\|\nabla\boldsymbol{u}\|^2 + \frac{1}{2}C_f(t). \quad (A11)$$

Now consider the final term in (A10)

$$\int_\Omega y(\boldsymbol{u} - \boldsymbol{e}_x)\cdot\frac{\partial\boldsymbol{u}}{\partial y}dx = \int_\Omega y(\boldsymbol{u} - \boldsymbol{e}_x)\cdot\frac{\partial}{\partial y}(\boldsymbol{u} - \boldsymbol{e}_x)dx$$

$$\text{(by parts)} = \int \left[y|\boldsymbol{u} - \boldsymbol{e}_x|^2\right]_{y=0}^\infty dxdz$$

$$- \|\boldsymbol{u} - \boldsymbol{e}_x\|^2 - \int_\Omega y(\boldsymbol{u} - \boldsymbol{e}_x)\cdot\frac{\partial}{\partial y}(\boldsymbol{u} - \boldsymbol{e}_x)dx.$$

$$\text{(by (3.3))} = -\|\boldsymbol{u} - \boldsymbol{e}_x\|^2 - \int_\Omega y(\boldsymbol{u} - \boldsymbol{e}_x)\cdot\frac{\partial\boldsymbol{u}}{\partial y}dx. \quad (A12)$$

Noticing that the final term on the right-hand side of (A12) is the same as the term on the left-hand side, these can be collected to show that

$$\int_\Omega y(\boldsymbol{u} - \boldsymbol{e}_x)\cdot\frac{\partial\boldsymbol{u}}{\partial y}dx = -\frac{1}{2}\|\boldsymbol{u} - \boldsymbol{e}_x\|^2. \quad (A13)$$

Finally, combining (A10) and (A13) gives the energy equation

$$\frac{1}{2}\frac{d}{dt}\|\boldsymbol{u} - \boldsymbol{e}_x\|^2 + \frac{1}{Re}\|\nabla\boldsymbol{u}\|^2 = \frac{1}{2}C_f(t) - \frac{1}{2}f(t)\|\boldsymbol{u} - \boldsymbol{e}_x\|^2. \quad (A14)$$

□

REFERENCES

BARTHOLOMEW, P., DESKOS, G., FRANTZ, R.A.S., SCHUCH, F.N., LAMBALLAIS, E. & LAIZET, S. 2020 Xcompact3D: An open-source framework for solving turbulence problems on a Cartesian mesh. *SoftwareX* **12**, 100550.

BIAU, D. 2023 Self-similar temporal turbulent boundary layer flow. *Comput. Fluids* **254**, 105795.

COLES, D. 1956 The law of the wake in the turbulent boundary layer. *J. Fluid Mech.* **1**, 191–226.

DAIRAY, T., LAMBALLAIS, E., LAIZET, S. & VASSILICOS, J.C. 2017 Numerical dissipation vs. subgrid-scale modelling for large eddy simulation. *J. Comput. Phys.* **337**, 252–274.

DEVENPORT, W.J. & LOWE, K.T. 2022 Equilibrium and non-equilibrium turbulent boundary layers. *Prog. Aerosp. Sci.* **131**, 100807.

DIAZ-DANIEL, C., LAIZET, S. & VASSILICOS, J.C. 2017 Wall shear stress fluctuations: mixed scaling and their effects on velocity fluctuations in a turbulent boundary layer. *Phys. Fluids* **29** (5), 055102.

DOERING, C.R. & CONSTANTIN, P. 1992 Energy dissipation in shear driven turbulence. *Phys. Rev. Lett.* **69**, 1648–1651.

EITEL-AMOR, G., ORLU, R. & SCHLATTER, P. 2014 Simulation and validation of a spatially evolving turbulent boundary layer up to $Re_\theta = 8300$. *Intl J. Heat Fluid Flow* **47**, 57–69.

FANTUZZI, G. & WYNN, A. 2016 Optimal bounds with semidefinite programming: an application to stress-driven shear flows. *Phys. Rev. E* **93**, 043308.

FERNHOLZ, H.H. & FINLEY, P.J. 1996 The incompressible zero-pressure-gradient turbulent boundary layer: an assessment of the data. *Exp. Fluids* **32**, 245–311.

KOZUL, M., CHUNG, D. & MONTY, J.P. 2016 Direct numerical simulation of the incompressible temporally developing turbulent boundary layer. *J. Fluid Mech.* **796**, 437–472.

KRAVCHENKO, A. & MOIN, P. 1997 On the effect of numerical errors in large eddy simulations of turbulent flows. *J. Comput. Phys.* **131**, 310–322.

KUMAR, A. & GARAUD, P. 2020 Bound on the drag coefficient for a flat plate in a uniform flow. *J. Fluid Mech.* **900**, A6.

LAIZET, S. & LAMBALLAIS, E. 2009 High-order compact schemes for incompressible flows: a simple and efficient method with quasi-spectral accuracy. *J. Comput. Phys.* **228**, 5989–6015.

LAIZET, S. & NING, L. 2011 Incompact3d: a powerful tool to tackle turbulence problems with up to $\mathcal{O}(10^5)$ computational cores. *Intl J. Numer. Meth. Fluids* **67** (11), 1735–1757.

LAMBALLAIS, E., FORTUNÉ, V. & LAIZET, S. 2011 Straightforward high-order numerical dissipation via the viscous term for direct and large eddy simulation. *J. Comput. Phys.* **230**, 3270–3275.

LELE, S. 1992 Compact finite difference schemes with spectral-like resolution. *J. Comput. Phys.* **103**, 16–42.

MAHFOZE, O.A. & LAIZET, S. 2021 Non-explicit large eddy simulations of turbulent channel flows from $Re_\theta = 180$ up to $Re_\theta = 5200$. *Comput. Fluids* **228**, 105019.

MOIN, P. & MAHESH, K. 1998 Direct numerical simulation: a tool in turbulence research. *Annu. Rev. Fluid Mech.* **30**, 539–578.

O'CONNOR, J., DIESSNER, M., WILSON, K., WHALLEY, R.D., WYNN, A. & LAIZET, S. 2023 Optimisation and analysis of streamwise-varying wall-normal blowing in a turbulent boundary layer. *Flow Turbul. Combust.* **110** (4), 993–1021.

PLASTING, S.C. & KERSWELL, R.R. 2003 Improved upper bound on the energy dissipation rate in plane Couette flow: the full solution to Busse's problem and the Constantin–Doering–Hopf problem with one-dimensional background field. *J. Fluid Mech.* **477**, 363–379.

VAN REEUWIJK, M. & HOLZNER, M. 2014 The turbulence boundary of a temporal jet. *J. Fluid Mech.* **739**, 254–275.

ROGERS, M.M. & MOSER, R.D. 1994 Direct simulation of a self-similar turbulent mixing layer. *Phys. Fluids* **6**, 903–923.

SCHLATTER, P. & ORLU, R. 2010 Assessment of direct numerical simulation data of turbulent boundary layers. *J. Fluid Mech.* **659**, 116–126.

SCHLICHTING, H. & GERSTEN, K. 2017 *Boundary-Layer Theory*. 9th edn, Springer.

SILLERO, J.A., JIMÉNEZ, J. & MOSER, R.D. 2013 One-point statistics for turbulent wall-bounded flows at Reynolds numbers up to $\delta^+ \equiv 2000$. *Phys. Fluids* **25**, 105102.

SMITS, A.J., HULTMARK, M., LEE, M., PIROZZOLI, S. & WU, X. 2021 Reynolds stress scaling in the near-wall region of wall-bounded flows. *J. Fluid Mech.* **926**, A31.

SPALART, P.R. 1986 Direct simulation of a turbulent boundary layer up to $re_\theta = 1410$.

TOPALIAN, V., OLIVER, T.A., ULERICH, R. & MOSER, R.D. 2017 Temporal slow-growth formulation for direct numerical simulation of compressible wall-bounded flows. *Phys. Rev. Fluids* **2**, 084602.